Technical Report
RAL-TR-1999-036

The Laboratory Calibration of the SOHO Coronal Diagnostic Spectrometer

J Lang B J Kent A A Breeveld E R Breeveld B J I Bromage
J Hollandt J Payne C D Pike and W T Thompson

18th May 1999

Enquiries about copyright, reproduction and requests for additional copies of this report should be addressed to:

The Central Laboratory of the Research Councils
Library and Information Services
Rutherford Appleton Laboratory
Chilton
Didcot
Oxfordshire
OX11 0QX
Tel: 01235 445384 Fax: 01235 446403
E-mail library@rl.ac.uk

ISSN 1358-6254

The Laboratory Calibration of the SOHO Coronal Diagnostic Spectrometer

J. Lang[1], B. J. Kent[1], A. A. Breeveld[2], E. R. Breeveld[2], B. J. I. Bromage[3], J. Hollandt[4], J. Payne[1], C. D. Pike[1] and W. T. Thompson[5]

[1]Rutherford Appleton Laboratory, Chilton, Didcot, Oxon OX11 0QX, UK
[2]Mullard Space Science Laboratory, UCL, Holmbury St Mary, Surrey RH5 6NT, UK
[3]University of Central Lancashire, Preston PR1 2HE, UK
[4]Physikalisch-Technische Bundesanstalt, D-10587 Berlin, Germany
[5]SM&A Corporation, 9315 Largo Drive West, Largo, MD 20774, USA

ABSTRACT

The laboratory end-to-end testing of the Coronal Diagnostic Spectrometer (CDS) experiment on the ESA/NASA SOHO mission is reported. A brief overview of CDS, which operates in the extreme ultraviolet wavelength range, is given. Pertinent details of the calibration source are presented, followed by an account of the source beam characterisation. A section is devoted to the determination of the instrument apertures and this includes an outline of the measurements, the results from both the grazing incidence and normal incidence aperture scans and their interpretation to yield estimated aperture areas. Next the measurement of spectrometer bandwidths and their comparison with expected values are described. Then the pre-launch wavelength calibrations are obtained. The section on sensitivity starts with an evaluation of the effects of polarisation on the measurements. The expected sensitivities are then derived. The measurements, their analysis and a comparison of measured and expected sensitivities are presented both for the normal incidence and grazing incidence spectrometers. The application of the laboratory calibration to in-flight solar data is discussed.

1 Introduction

The CDS experiment was built by an international consortium led by the Rutherford Appleton Laboratory. The final assembly, integration, test and calibration of the payload was carried out at the Rutherford Appleton Laboratory at the beginning of 1994 just prior to final delivery of the hardware for integration to the payload module. The calibration provided an end-to-end test of the whole CDS subsystem as it involved illuminating CDS with suitable extreme ultraviolet (EUV) radiation at the CDS input and checking the output after the CDS subsystem spacecraft interface. In fact as CDS was used with a spacecraft simulator and sophisticated ground support equipment, the test operations were conducted similarly to flight operations. The source of EUV radiation was a secondary standard, a hollow cathode combined with a collimating telescope, which had been calibrated against an electron storage ring primary standard. The principal aims of the tests were to provide both wavelength and responsivity calibrations. However, as the source beam did not fill the CDS aperture it was necessary to map the apertures with the source. In addition the cross section of the source beam had also to be determined.

This report contains a brief overview of CDS (section 2) followed by descriptions of the source in section 3 and its characterisation in section 4. The determination of the apertures, including estimates of their areas are discussed in section 5. The measurements of the spectrometer bandwidths are presented in section 6. Section 7 is devoted to the wavelength calibration and section 8 to the measurements of the sensitivities of the spectrometers. The response of CDS to polarised radiation is also discussed in section 8. The application of the laboratory calibrations to in-flight measurements is contained in section 9 and the conclusions are in section 10.

2 Overview of CDS

A full description of the CDS scientific objectives and flight hardware is given in the paper by Harrison et al. (1995). Here details pertinent to the calibration are summarised. The optical layout of CDS is shown in figure 1 and its principal characteristics in table 1. CDS is a combined telescope dual spectrometer and consists of a Wolter-Schwarzschild II grazing incidence telescope focused at the common entrance slit of a pair of spectrometers via a plane scan mirror. Although the telescope is constructed as a full figure of revolution, two apertures immediately in front of the telescope, together with light stops behind, define two different optical paths which illuminate the two spectrometers through the slit assembly. The field of view is 4 arc-minutes by 4 arc-minutes and, to give coverage of the whole Sun, the entire instrument can be moved on articulated legs.

In the normal incidence spectrometer (NIS) component of CDS the incoming beam is incident on a pair of toroidal gratings at near normal incidence. As the spectrometer is stigmatic, the diffracted image of the entrance slit (whose length in flight is usually aligned to the solar N-S direction) is formed on the two-dimensional detector. The two gratings are slightly tilted with respect to each other such that the two spectra can be detected simultaneously, one above the other. By moving the scan mirror in the E-W direction images can easily be obtained. The NIS detector is an intensified CCD known as the VDS (Viewfinder Detector System) and is described by Thompson et al. (1992). Solar photons dispersed by the grating are incident on a windowless microchannel plate (MCP). The resulting electron cloud at the output of the microchannel plate is converted to visible light by a phosphor-coated fibre-optic window. This visible light is then focused by a lens on to a passively cooled 1024×1024 CCD with 21 μm pixels. During the calibration, the CCD was read out in its

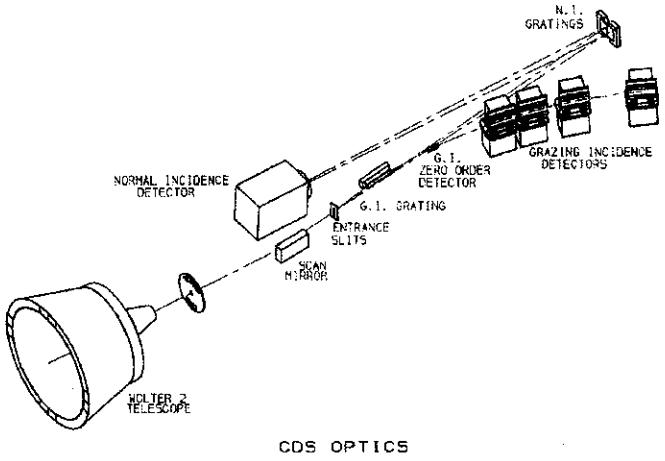

Figure 1: The Coronal Diagnostic Spectrometer optical layout

nominal mode simultaneously through all four quadrants. In flight, this was changed to one of the back-up modes to read through only two quadrants to avoid noise from the cross-talk between the other two quadrants. After an exposure the MCP is gated off and between the end of the exposure and the next read there is a 0.1 s wait to ensure the MCP voltage has decayed completely. Spectral regions are selected by 'windowing', the read out time being 14 μs for each in-window pixel and 2 μs for each discarded pixel. To read and retain a full image takes 3.7 s and to flush (discard) a CCD image takes 0.5 s.

In the grazing incidence spectrometer (GIS) part of CDS light from the slit illuminates a spherical grating at grazing incidence and is then dispersed on to four separate one dimensional detectors at fixed positions on the Rowland circle. For this astigmatic spectrometer spatial information can be obtained by using square 'pinhole' slits and rastering by moving both the scan mirror (for E-W solar motion) and the slit (for N-S solar motion) to build up the required spatial pattern. The GIS detectors each consist of a triple 'Z' stack of MCPs with 'spiral anode' (SPAN) readouts and are described by Breeveld et al. (1992) and Breeveld (1995). The active area of each detector is 50.0 mm $\times$ 16.6 mm with effectively 2048 resolution elements (pixels) of size 25 μm $\times$ 16.6 mm. The pixel data are recorded in an array of 8192 elements, detector 1 using pixels 0 - 2047, detector 2 pixels 2048 - 4097 etc. For each detector the wavelength decreases with increasing pixel number for the configuration used for the calibration. For the flight data, the pixels are reversed by the ground software, so that wavelength increases with increasing pixel number.

A solar photon incident on the front of the MCP stack produces a cloud of electrons at the rear. The number of electrons produced by one photon is the gain of the event and these gains have an approximately normal distribution, called the pulse height distribution (PHD). The position of the peak of this distribution is the modal or detector gain. Only a certain range of event gains are processed by the electronics and these are determined by upper and lower level discriminators (ULD and LLD).

The SPAN anode system produces two digital signals whose magnitudes depend on the photon arrival position. These signals after processing are used in a look up table (LUT) to give the

Telescope and mechanism details	Outer f-number	9.38
	Effective focal length	257.831 cm
	Plate scale at slit	12.5 μm/arc-sec
	Full geometric area	289.28 cm^2
	Field of view	4 x 4 arc-min^2
	PSF[1] FWHM	$\sim$ 2 arc-sec
	Pointing	Anywhere on disc and low corona
	Step sizes	E - W = 2.032 arc-sec (mirror)
		N - S = 1.016 arc-sec (slit)
The NIS	Telescope aperture	34.3 cm^2 per grating
	Wavelength range	308 - 381 Å, 513 - 633 Å
	Prime slits (4, 5, 6)	2 $\times$ 240, 4 $\times$ 240, 90 $\times$ 240 arc-seconds^2
	Grating ruling	2400 and 4000 l/mm
	Slit-grating distance	736.5 mm
	Grating-detector distance	744.6 mm
The GIS	Telescope aperture	47 cm^2
	Wavelength range	151- 221 Å, 256 - 338 Å
		393 - 493 Å, 656 - 785 Å
	Prime slits (1, 2, 3)	2 $\times$ 2, 4 $\times$ 4, 8 $\times$ 50 arc-sec^2
	Grating ruling	1000 l/mm
	Rowland circle radius	750 mm
General	Total mass	100 kg
	Overall length	1.7 m
	Average power	58 W
	Telemetry rates	11.3, 22.6, 1.9 kbit/s

[1]PSF = Point Spread Function, the distribution expected when imaging a point source.

Table 1: Basic CDS characteristics

appropriate pixel position for the photon. Each detector has a separate LUT which can be re-built to match the detector outputs. To calculate each position in real time without a LUT takes too long at the working count rates. To choose a LUT, anode signals are sent to the ground as raw data. A data spiral pattern is fitted to the raw data and the 11 parameters are selected to rebuild the LUT. A poor fit of the LUT to the output can lead to loss of data, or ghosting into incorrect pixels.

The detector readout electronics are designed to operate at up to 1×10^5 counts/s. There is a measured analogue extending dead time of 2.1 μs, which can be corrected using standard equations. However, the GIS to CDHS (Command and Data-Handling System) link can only work at a maximum constant rate of 8.9×10^4 counts/s, for the combined output of the four detectors. Any data above this count rate are lost. A first-in/first-out register to de-randomise data passed to the link introduces a non-extending dead time of 10 μs to the combined detector output. At combined count rates above the maximum, approximately half the data from the detectors are lost. Thus at (combined) count rates above 5×10^4 counts/s the real total count rate is ambiguous.

Electrons emitted when the two tungsten filaments mounted in front of the detectors are powered (and the bias at the front of the detectors is reversed) can initiate detector events. This allows checks for regions of reduced efficiency due to long term gain depression as well as front-to-back detector tests.

To allow CDS to operate fully a vacuum was required. The contamination control requirements, particularly for the optics and detectors, were a partial pressure at 43 amu of $< 5 \times 10^{-9}$ torr and particulate control to class 100. The vacuum chamber housing CDS was made of cleaned stainless steel (2 m long x 1 m diameter) pumped by a 2000 l/s turbomolecular pump used with a liquid nitrogen cooled chevron baffle to prevent any possibility of contamination return from the pumping system.

Three workstations were used to operate CDS during the calibration. Commands were sent to and telemetry received from CDS via a spacecraft simulator. The manning and style of operation was just as envisaged for flight, with staff assigned for actual operations and others used to make the calibration plans and analyse the data. The experience gained was valuable for mission planning.

3 The calibration source

A high current, hollow cathode source (Danzmann et al. 1988) was used to produce the EUV line radiation necessary for the calibration. It is an extremely stable source when operated at calibrated set points of voltage (400 V), current (2 A) and buffer gas pressure (0.5 to 2 mbar depending on the gas). The source emits unpolarised line radiation from the buffer gas and sputtered cathode material (99.5% aluminium). Radiation from the 1 cm diameter hollow cathode is stopped down by a 0.6 mm diameter pinhole at the focus of a Wolter II telescope used to provide a collimated output beam from the hollow cathode. This output beam from the source i.e. hollow cathode/telescope combination is restricted by a beam stop to 5 mm diameter.

The calibration source is in fact a secondary standard having been radiometrically calibrated using a primary standard of radiation, the BESSY electron storage ring operated in Berlin, Germany by Physikalisch-Technische Bundesanstalt. The calibration is described by Hollandt, Künhe and Wende (1994) and Hollandt et al. (1996a). The wavelengths and intensities of the calibrated lines from the source are given in table 2.

Wavelength/Å	Species	Detector	Photon flux (photons/s)
160.1/161.7	Al IV (Ne)	GI1	5.43×10^4
169.5 - 175.6	Al III (Ne)	GI1	1.22×10^5
160.1/161.7	Al IV (Ar)	GI1	4.86×10^4
169.5 - 175.6	Al III (Ar)	GI1	8.77×10^4
204.3 - 208.9	Ne IV	GI1	3.43×10^5
212.6	Ne IV	GI1	1.23×10^5
215.4 - 218.8	Ne IV	GI1	4.81×10^5
222.6 - 223.6	Ne IV	GI1	2.03×10^5
267.1 - 267.7	Ne III	GI2	1.01×10^6
282.5 - 283.9	Ne III	GI2	2.61×10^6
301.1	Ne III	GI2	1.55×10^6
303.8	He II	GI2	4.89×10^7
308.6	Ne III	GI2	6.21×10^5
313.1 - 313.9	Ne III	GI2/NI1	1.96×10^6
319.5 - 320.0	Ne II	NI1	1.87×10^6
324.6 - 331.5	Ne II	NI1	1.06×10^7
352.2 - 357.5	Ne II	NI1	1.38×10^7
361.4 - 362.5	Ne II	NI1	7.84×10^6
379.3	Ne III	NI1	1.09×10^7
405.9/407.1	Ne II	GI3	2.01×10^7
445.0 - 447.8	Ne II	GI3	3.89×10^7
460.7 - 462.4	Ne II	GI3	1.57×10^8
488.1 - 491.1	Ne III	GI3	1.75×10^7
537.0	He I	NI2	7.16×10^6
542.9 - 543.4	Ar II	NI2	$3.84 \times 10^{6*}$
547.5	Ar II	NI2	$5.17 \times 10^{6*}$
583.4	Ar II	NI2	$1.16 \times 10^{6*}$
584.3	He I	NI2	1.79×10^8
567 - 592	Ar II	NI2	9.87×10^6
592 - 622	Ar II	NI2	4.72×10^6
718.1 - 745.3	Ar II	GI4	2.54×10^7
735.9	Ne I	GI4	1.00×10^8
743.7	Ne I	GI4	5.88×10^7
769.2	Ar III	GI4	2.25×10^6

Table 2: Source calibration line list from Hollandt et al. (1996a) and Hollandt (1994). For the Al III and Al IV lines the buffer gas is also indicated. The detectors are numbered from short to long wavelength for both GIS and NIS. The derivation of the fluxes marked with a * is described in section 8.3.1.

Since it was not possible to fill the CDS aperture using the calibration source, the calibration system was designed to allow the source and CDS to be moved relative to each other so that a map of the response over each of the apertures could be obtained. This of course is not a perfect solution as any calibration source (whether it under, over or just fills the aperture) will be different to the Sun in terms of spatial structure, angular spread and have a fixed intensity while the solar line radiation does not.

Radiation from the calibration source entered the tank by one of two ports, the upper one providing illumination of the NI aperture and the lower, the GI aperture. Alignment of the source to CDS made use of a visible laser beam. This was projected through the hollow cathode and telescope and was thus coaligned with the EUV beam. Two windows each 100 mm diameter on each side of the centre line between the two ports, allowed both an autocollimator attached to the source platform to view an optical flat attached to CDS and a second alignment laser also attached to the source platform to illuminate an 'aperture map'. This 'map' was a coarse location grid mounted on the CDS support structure, representing the grid system defining the positions in the aperture (see later).

The source pencil beam was focused by the CDS telescope via the scan mirror on to the plane of the spectrometers' entrance slits which are all on a common plate which can be moved by an x-axis (vertical in the laboratory) translation. Ideally the beam should pass through the largest slit without loss for photometric calibration. The narrowest slits, providing the highest spectral resolution, were used for wavelength calibration.

Typical spectra for the normal and grazing incidence detectors are shown in figures 2 and 3.

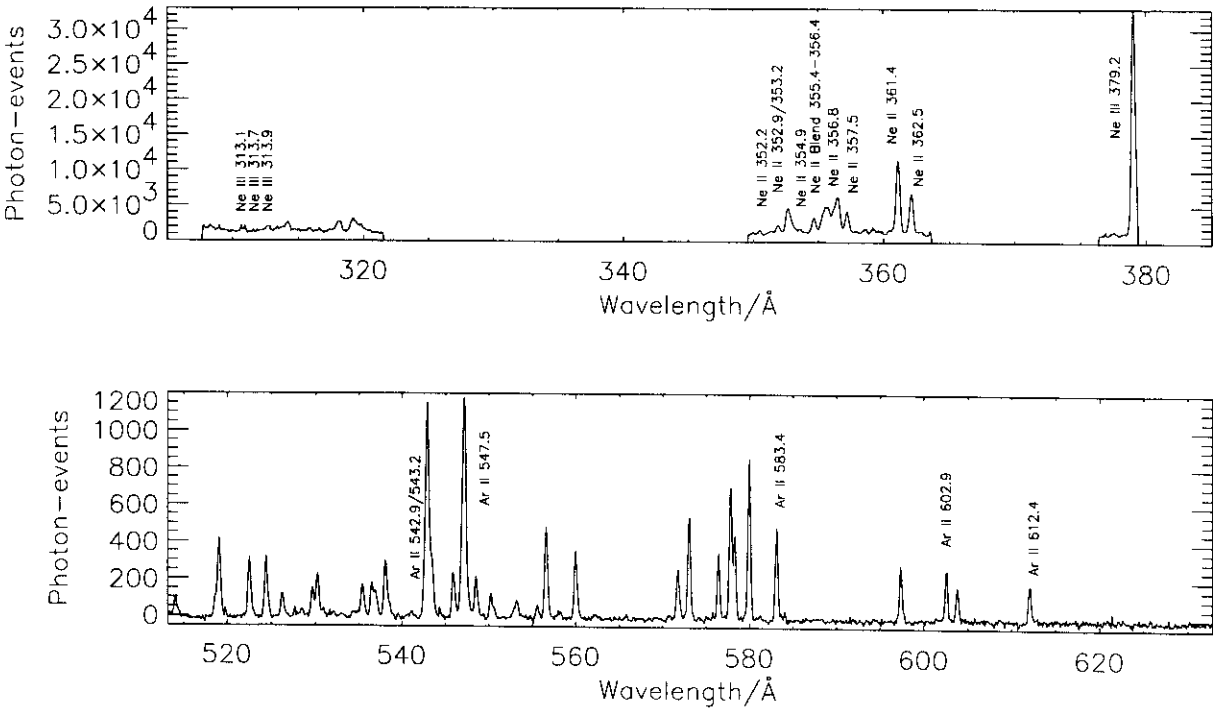

Figure 2: Hollow cathode source spectra of argon and neon from the NIS using slit 4. The upper short wavelength channel shows an example of data windowing.

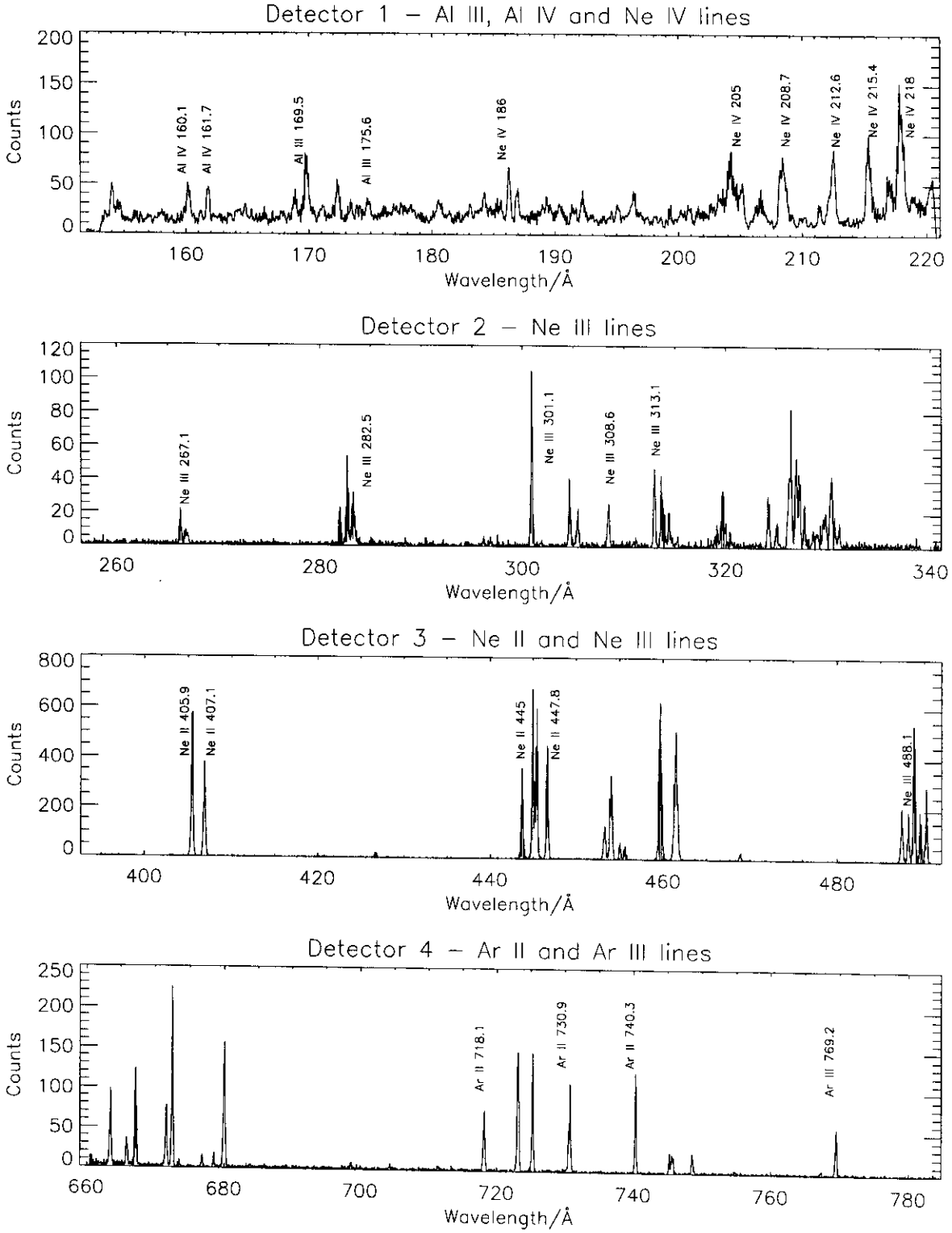

Figure 3: Hollow cathode source spectra of aluminium, argon and neon from the GIS using slit 4.

4 Source beam characterisation

To establish the size and intensity distribution of the source beam, the beam spot was scanned in two perpendicular directions at the entrance slit.

Firstly the focused beam was passed over the 25 μm $\times$ 3 mm slit 4 (2 arc-sec $\times$ 240 arc-sec) by rotating the scan mirror in single (2 arc-sec) steps. The intensity of radiation passing through the slit was measured in the GIS by taking the sum of all the counts in the longest wavelength channel (detector 4, 656 - 785 Å). As the hollow cathode was operated using neon this was effectively the sum of the intensities of the Ne I 735.9 Å and 743.7 Å lines. An image was obtained using the NIS with slit 6 (1.125 mm $\times$ 3 mm). The results are shown in figure 4, essentially the same profile being obtained for each spectrometer, with the NIS profile being curtailed by the slit edges. The distribution extends over the entire scan mirror range of ± 2 arc-min from a source which is nominally collimated to better than one arc-min, assuming an ideal telescope and alignment of the source in respect to the telescope. Figure 5 shows the line profile from the GIS for the Ne I 735.9 Å line for each of the scan mirror positions. The spectral line position changes. This is a direct result of the source beam not filling the telescope aperture.

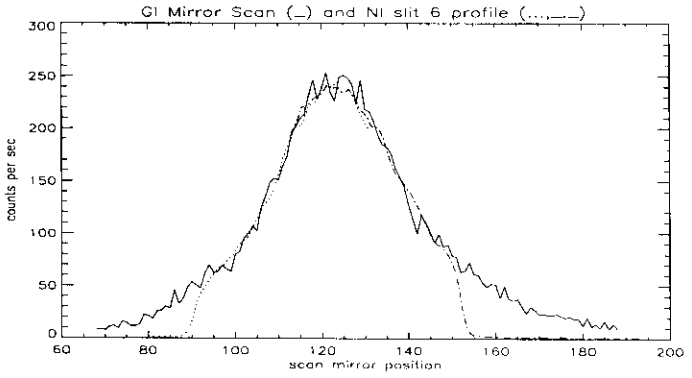

Figure 4: Source profile from a mirror scan using the GIS (—) and from the NIS (spatially summed). For the NIS the profile is wider than the widest slit so two scans were combined.

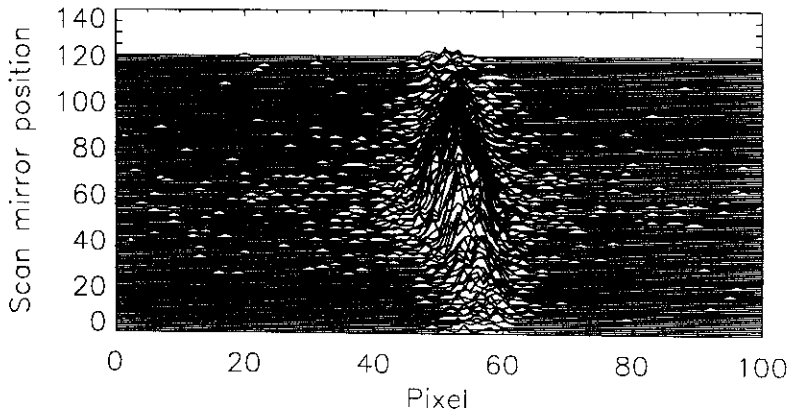

Figure 5: Profile of the Ne IV 735.9 Å line for each position of the mirror scan using the GIS

Secondly, 'pinhole' square slits were scanned over the beam spot in a direction perpendicular to that scanned by the scan mirror i.e. perpendicular to the dispersion direction. In this case the results using the GIS with detector 4, as given in figure 6, showed that the peak spectral line position remained fixed for a particular slit scan but changed for slit scans carried out at different scan mirror positions as expected from the scan mirror case.

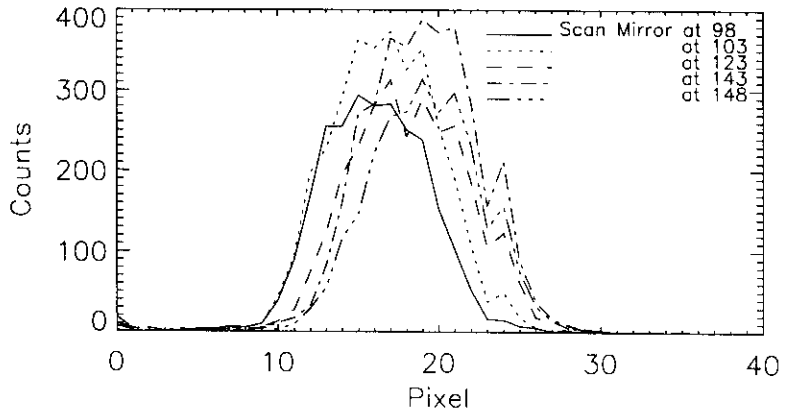

Figure 6: Profile of the GIS Ne IV 735.9 Å line summed over the central 20 slit positions for each of 5 scan mirror positions.

The elliptical form of the source aperture indicated by the GI scans is confirmed by the shape of the image produced on the NI detector, as shown in figure 7.

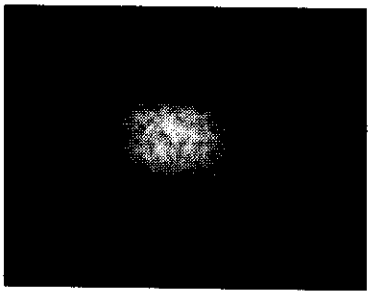

Figure 7: The intensity image profile of the source the He I 584.3 Å line, obtained from the NIS with slit 6.

Measurements were made to investigate why the width of the source profile with scan mirror position was larger than expected. A high resolution imaging detector was used to obtain spatial images of the calibration beam before it entered the CDS telescope. These images showed structure (Kent et al. 1999), the various features being stable with time and present under all source operating conditions. By taking images at different distances from the calibration source and noting that the features remained but changed in scale, a beam angular divergence of ± 1.85 arc-minutes was derived. This explains the extended profile observed from the mirror scan.

5 Aperture determination

The size which is actually used of either CDS aperture is determined by a combination of the physical aperture and the effects of various beam stops and masks in conjunction with the other optical elements. As the source beam is smaller than either aperture the apertures must be mapped to obtain their areas for the intensity calibration. Theoretical apertures have been calculated using the CodeV[1] ray-tracing software (Lidiard (1995) and Lidiard and Gray (1997)). The shape and size of the used aperture changes with scan mirror position so the calculations were done for three positions, the middle and the two extremes, corresponding to mirror positions 128, 68 and 188. These theoretical apertures are shown in figures 8 and 9. The NI aperture is split into two halves, one for each grating and are referred to as the NI1 and NI2, for the short and long wavelength ranges respectively.

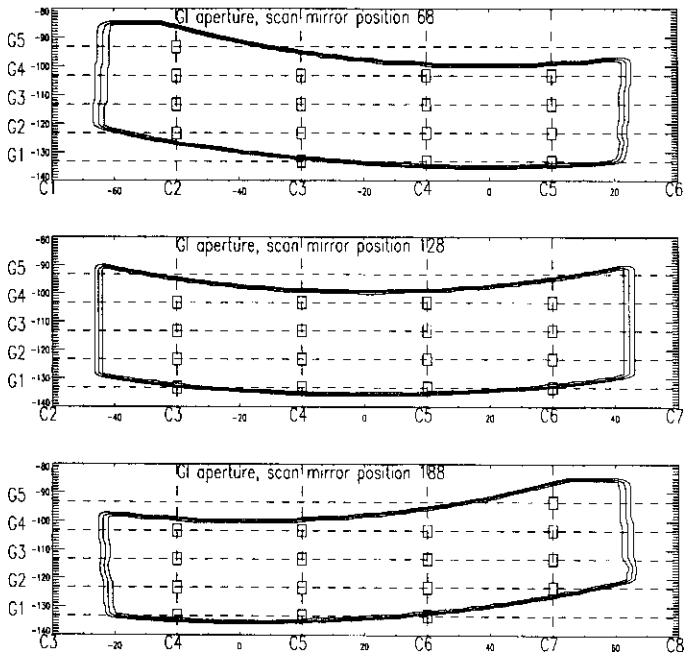

Figure 8: Grazing incidence theoretical apertures for three scan mirror positions with the scales of the graphs in mm. The outer contour indicates where radiation will be detected as the test beam (5 mm diameter and non-diverging) using slit 4 is scanned into the aperture. The middle and inner contours indicate the half and full illumination loci respectively.

The calibration source beam, of cross-section about 5 mm at the CDS apertures, was scanned horizontally across the apertures in an attempt to delimit the boundaries. For the GI aperture the step size was 2.5 mm and five horizontal scans, separated vertically by about 10 mm, corresponding to grid positions marked G1 to G5 in figure 8, were carried out for scan mirror positions 68, 128 and 188. The variation in counts obtained, using slit 4, in one or two strong lines was plotted against aperture position. Unfortunately, because of test equipment failures compounded by time shortages, scans for the NIS were done using slit 2 at the central mirror position and with 5 mm steps. Only three scans were carried out, for grid positions (as defined in figure 9) N3 (partially), N4 and N5 for NI1 and a single vertical scan for NI2.

[1]CodeV is a registered trademark of Optical Research Associates, Pasadena, California, USA

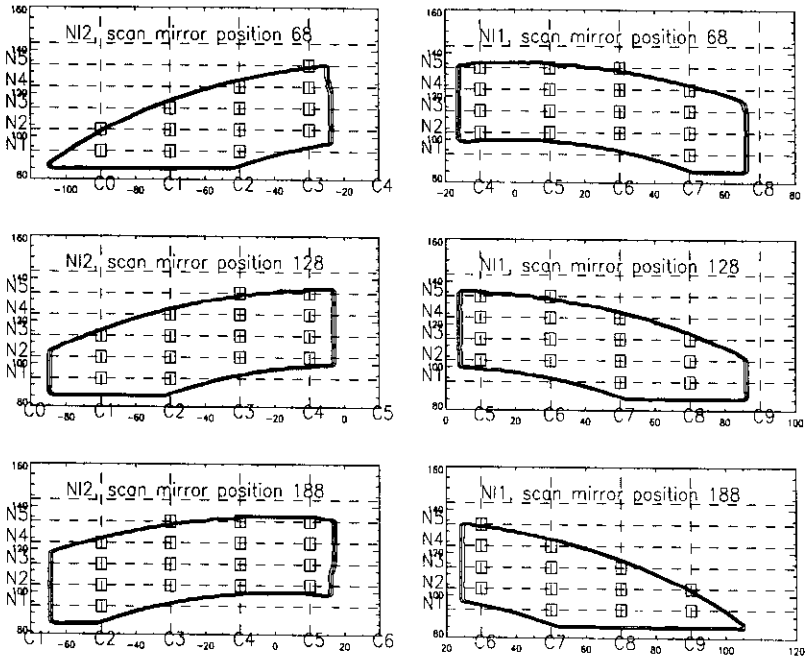

Figure 9: Normal incidence theoretical apertures for three scan mirror positions with the graph scales in mm. The outer contour indicates where radiation will be detected as the test beam (5 mm diameter and non-diverging) using slit 4 is scanned into the aperture. The middle and inner contours indicate the half and full illumination loci respectively.

5.1 Results from aperture scan measurements

It was expected that each scan would yield a profile that was essentially a 'top-hat' shape, with sides which sloped over a horizontal distance of about 7 mm, because of the finite size of the beam and the 'width' of the boundary, plus small 'wings' due to scattering at the edges. The central region (corresponding to the part of the scan where the whole of the beam passed through the aperture) was expected to be a smoothly changing but not necessarily flat function, due to reflectivity differences as the grazing angle changes in traversing the telescope.

5.1.1 Results from the GI aperture scans

The results of the GI aperture scans are given in figure 10. Comparisons of scans at the same positions but at different wavelengths showed that the aperture size did not depend on wavelength.

Observations as the beam crossed the curved regions of the boundary, which are defined by the telescope exit aperture and are independent of scan mirror position, were as expected.

Interestingly the positions of the lines on the detectors were seen to shift as the aperture was scanned (see also figure 22), the shift being smaller for the normal incidence data.

The CodeV software was used to investigate these line shifts. Rays incident parallel to the telescope axis but spread across the aperture were traced through the system to the detectors. The results are shown in figure 11. The shift in position of the light passing near the edges of the aperture is

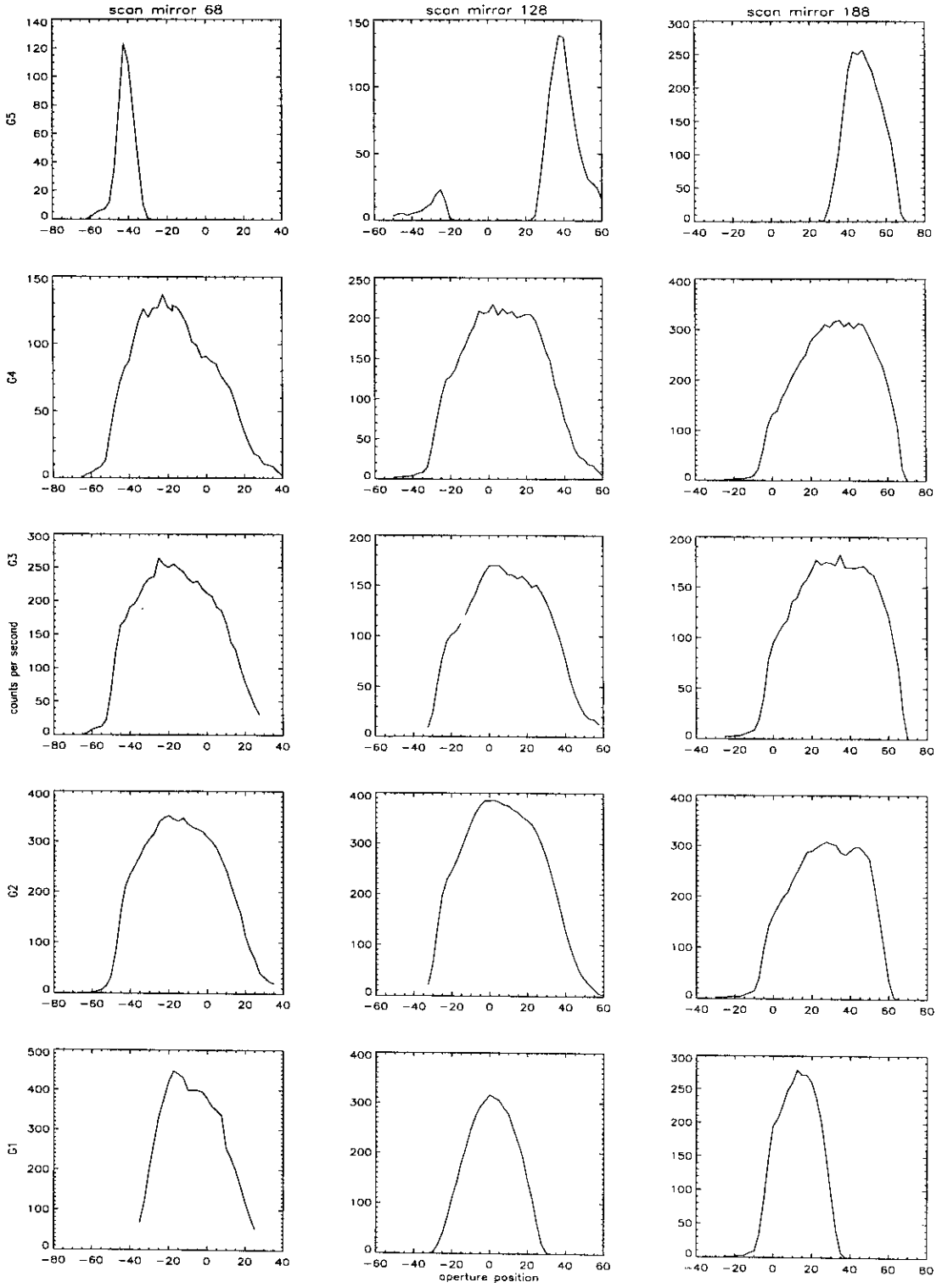

Figure 10: Grazing incidence aperture scans, the aperture positions being in mm units.

expected to have a broadening effect on the observed lines when the full aperture is illuminated in flight. This may increase the line width by up to about 15%, for the narrowest lines, although without more ray-tracing to show the shift as a function of wavelength it is difficult to estimate precisely.

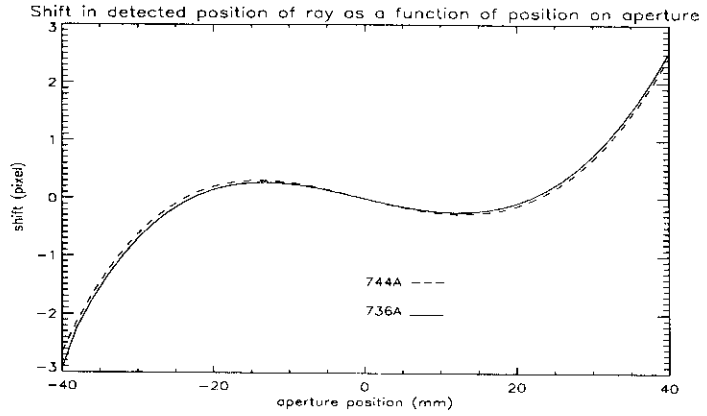

Figure 11: Results of the ray tracing calculation showing the variation in the pixel position at detector GI4 for a ray parallel to the optical axis as a function of position on the aperture.

The same CodeV calculation allowed the transmission of the system as a function of aperture position to be calculated, as shown in figure 12 for GI detector 4. This variation must be accounted for in the responsivity calibration with the narrow source beam as aperture position +10 mm was used for normalisation and reference and this corresponds to a minimum in transmission. For a fully illuminated aperture the correction factor is estimated to be 1.04±0.01. The uncertainty in the correction is taken as 25% i.e. (4±1)% and includes some allowance for any change with wavelength.

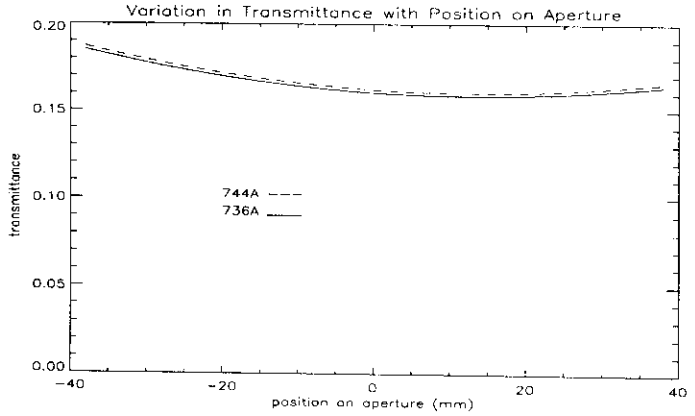

Figure 12: Results of a ray tracing calculation of the variation in transmission as a function of position on the aperture for a ray parallel to the optical axis and detected by detector GI4.

Considering the results shown in figure 10, there was no smooth central region, there was generally a small shoulder to the left (i.e. lower aperture position) about half-way up to the peak and the left-hand rise was about 16 mm to the right of its expected position. The right-hand side sloped too gradually, with measurable signal detected beyond the expected boundary.

	Mirror position		
Vertical position	68	128	188
G5	-	-	-
G4	0.59	0.59	(0.41)
G3	0.63	0.60	0.58
G2	0.63	0.60	0.63
G1	-	-	(0.69)

Table 3: Ratio of shoulder height to peak value in aperture scans. A - indicates that there was no shoulder apparent and values in brackets are affected by the aperture. The mean ratio is 0.61 ± 0.02.

The ratio of the shoulder height to that of the peak is given in table 3 and is constant apart from places where the beam is affected by the edges of the aperture. Alignment of the beam was carried out at aperture positions -10, +10 and +30 mm for all three mirror positions, the source having been correctly aligned in the direction perpendicular to the slit, with the source centred on the vertical axis of the slit. The shoulder is attributed to a change in alignment as the source was traversed from its aligned position. Although tests on the scanning mechanism showed that it maintained the direction of the incident radiation to within 10 arc-sec, a change in direction could affect the resultant profile which, of course, is a convolution of the source profile and the aperture profile. At the shoulder position the count rate has fallen by about 40%, and from the source profile (figure 4) corresponds to about 15 mirror steps from the centre. This implies a rate of movement of the source across the slit of about 0.5 mirror steps on the source for every mm moved across the aperture. This is larger than expected but could be enhanced by the shift in detected pixel position for rays passing near the edge of the aperture. Full confirmation would need a large effort with ray tracing, including off-axis rays. However, the results of a simulation support the conclusion. A program was written to deconvolve the source movement effect. Two parameters, the first representing the source profile and the second the rate of movement of the source across the slit were varied till a 'top hat' profile was achieved. The values of the parameters were consistent with the explanation especially the second which ranged from 0.5 to 0.6 c.f. 0.5 inferred above. The corrected profiles are shown in figure 13.

The peak count rates from the scans shown in figure 10 are given in table 4. There is no consistency in the peak count rates at the different positions. At these positions the radiation through the slit should be maximum with the source image aligned horizontally to be central on the slit. Checks on the source and CDS operating conditions ruled out source or instrument changes. A possible explanation is that the source image was not aligned vertically to be central on the slit. Evidence for this had been found using the NI, when the image did not fall on the slit (1 or 2) at all. A scan with slit 2 at position G2 instead of slit 4 (as in table 4) gave peak count rates consistent with the change of slit.

The left hand boundary at each mirror position is about 16 mm to the right of its expected position (at -47, -28 and -4.5 mm for mirror positions 68, 128 and 188, respectively). This is probably caused by a displacement of 0.5 mm of the grating mask defining this boundary. Such a displacement will not affect the NI optical path.

The right hand boundary slopes more gently than predicted in most cases, although for mirror position 188 there appears to be an additional steeper slope. The displacement of the grating mask

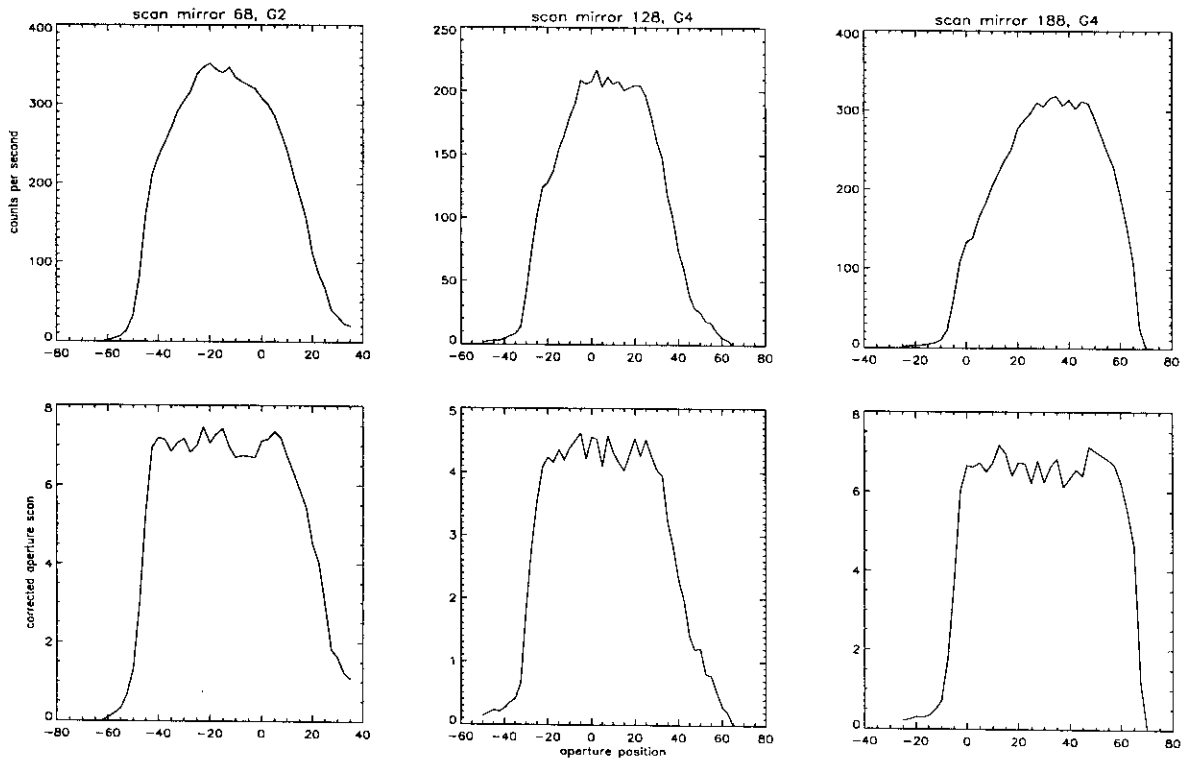

Figure 13: Upper row, GI aperture scans; lower row, the same scans corrected for movement of the source across the slit. The aperture positions are in mm units.

	Mirror position		
Vertical position	68	128	188
G5	135	160	263
G4	145	220	330
G3	270	166	190
G2	363	400	320
G1	460	310	290

Table 4: Variation with aperture position of the peak count rate (counts/s) during the aperture scans.

should move this boundary as it does for the left hand boundary, except that other parts of the optics or structure probably intervene. The result is a 'broader' boundary within a mm or two of the predicted position (at 22, 42, 65 mm for mirror positions 68, 128 and 188 respectively).

It can be concluded that the grazing incidence aperture scans are understood. The boundaries have been established and the reasons for the shoulder and the variations in peak count rate explained.

5.1.2 Results from the NI aperture scans

The signal to noise ratios in the NI results are not as good as for the GI results, principally because the VDS noise was greater than in flight as the detector was not cooled, increasing the thermal background. In addition the signal plus noise had to be kept below the saturation level, limiting the exposure time.

The results for the NI1 aperture scans are shown in figure 14. The upper and lower boundaries appear to be in the positions predicted by the ray tracing. The left hand (i.e. smaller aperture positions) edge at $+8\pm2$ mm appears displaced to the right by about 4 mm. From the N3 scan the right hand boundary does not occur before +70 mm. There is no experimental evidence for a shift of this boundary. However, as the left hand boundary appeared shifted, the same shift will be assumed for the right hand edge when estimating the aperture areas.

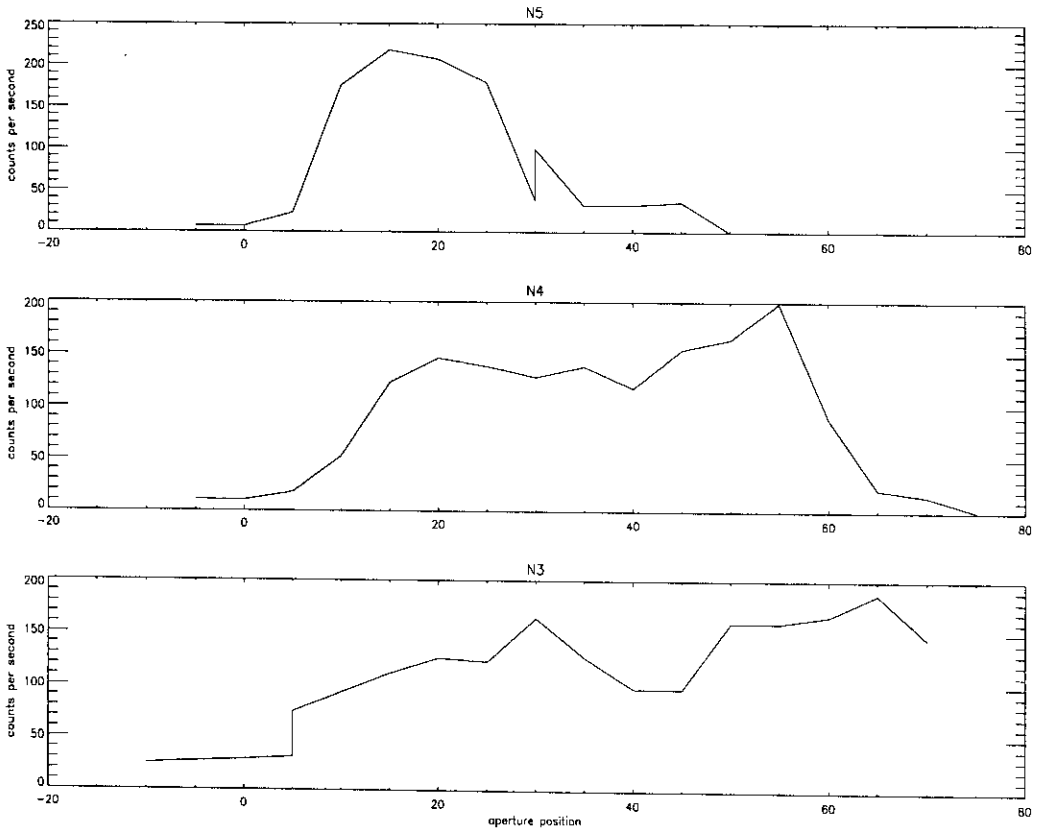

Figure 14: NI1 aperture scans. The first two points of the N5 scan have been corrected for the effect of spikes caused by bad telemetry packets. The positions are shown in mm units.

The results for the NI2 aperture scan are shown in figure 15. This is a vertical scan at horizontal

position -48 mm where the translation mechanism stuck in the test equipment and the spacecraft schedule did not allow time for it to be repaired. Indeed, maintaining the source alignment during the scan was also difficult and caused the source intensity to appear reduced. Most of the higher count rate points are affected by saturation and there were bad telemetry points resulting in a distorted profile. The upper and lower boundaries are as expected. In spite of the difficulties it was possible to measure the aperture areas.

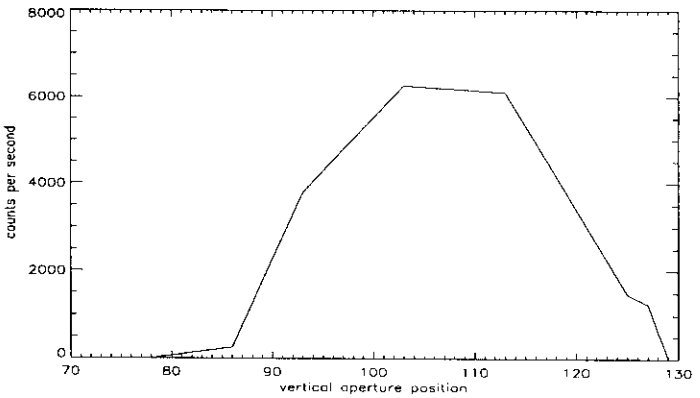

Figure 15: NI2 vertical aperture scan in mm units, at scan mirror position 144. The points around the peak are lower limits as the detector was saturated.

5.1.3 Estimated aperture areas

The estimated areas of the apertures are given in table 5. Considering the measurements and the difficulties just described, the uncertainties in the areas are reasonable. The fact that the differences in peak count rates are understood and that they should in fact all be the same gives confidence in establishing the uncertainties. While evaluating the uncertainties it was noted that the curved boundaries of the apertures were found as predicted. The smaller dimension of each aperture is measured better than the larger one. Its percentage uncertainty is estimated to be about half that of the larger dimension. In evaluating the uncertainty for the larger dimension for the GIS, the small shoulder on the profile helped define one boundary.

	Mirror position		
Aperture	68	128	188
GI	25.1 ± 0.9	25.5 ± 0.9	24.9 ± 0.9
NI1	29.1 ± 1.3	26.9 ± 1.3	22.3 ± 1.3
NI2	24.0 ± 2.0	28.0 ± 2.0	30.0 ± 2.0

Table 5: Estimates of the effective area (cm^2) of each aperture for the three scan mirror positions.

6 Spectrometer bandwidths

6.1 GIS

The flat faces of the GI detectors are mounted so that the centre line in the dispersion direction intersects the Rowland circle at two points. The resolution of the image of a point source (the point-spread function PSF) at any point on a detector depends both on the distance from the grating and from the Rowland circle. The expected widths of the PSFs for detectors 1 and 4 (Lidiard 1995) are shown in figure 16. The expected line width (full-width half-maximum FWHM) for the same detectors for slits a factor two different in width are given in figure 17.

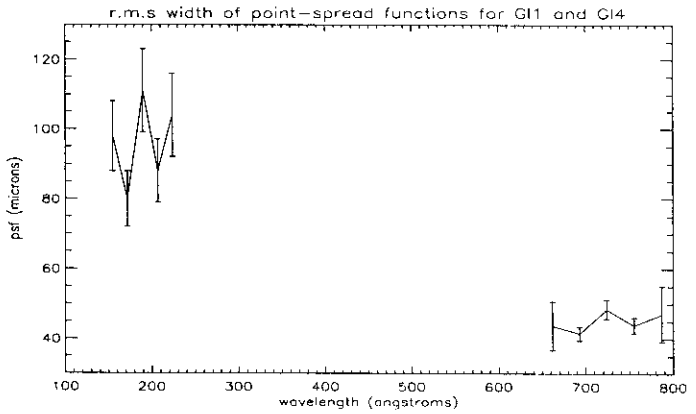

Figure 16: Predicted r.m.s. focal line width of the point-spread function as a function of wavelength for detectors GI1 and GI4.

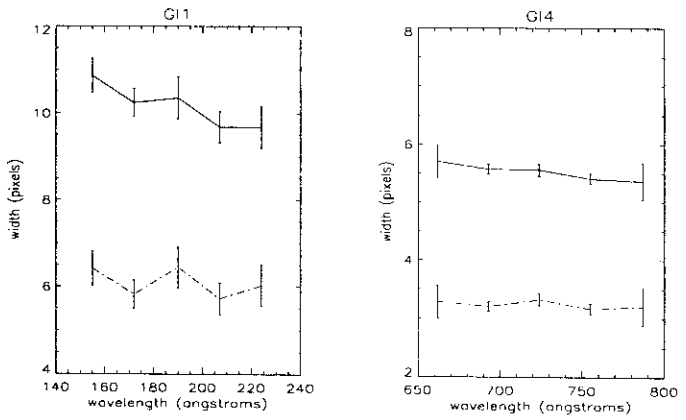

Figure 17: Expected line FWHM for GIS detectors 1 and 4. The solid line shows values for 50 μm slits (2 and 5) and the broken line values for 25 μm slits (1 and 4).

Analysis of the measured line widths was complicated by the problem of 'fixed patterning'. This arises with position sensitive detectors where the charge falling on the anode is divided before being digitised to determine the position. Because the anode charges have probability distributions and are essentially continuous quantities and analogue to digital converters are used to produce integer quantities, in effect an analogue equation is being solved using integer arithmetic (Geesmann et al. 1991). This manifests itself as an excess of counts in certain bins and a corresponding decrease

in counts in other bins. The position of the fixed patterning depends on the look-up table used. However, the total counts observed are conserved. A sample of the effects such fixed patterning can have on line profiles is shown in figure 18. The line positions and widths were obtained for all four GIS detectors and the results for GI1 and GI4 are shown in figures 19 and 20. The figures include the spectra analysed to help assess the effects of the fixed patterning.

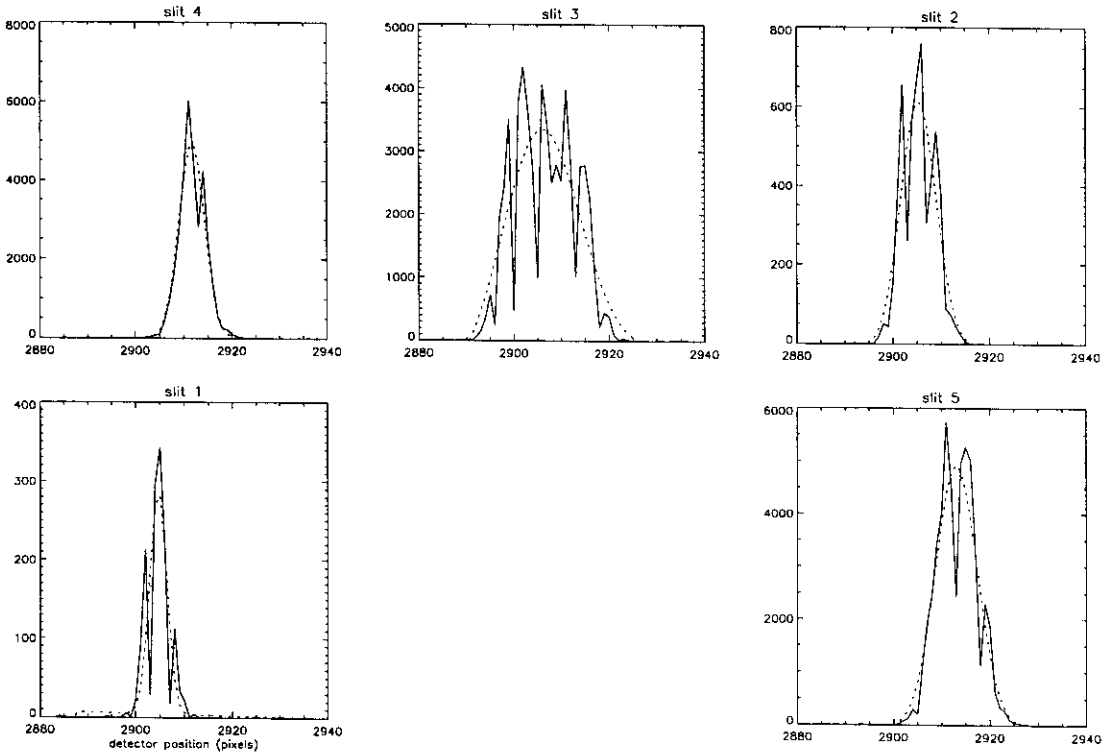

Figure 18: An illustration of the effects of fixed patterning for the He I 303.8 Å line observed using different slits. The ordinate is in units of counts/pixel and the dashed lines show Gaussian fits to the measured profiles.

Using slits of the same width, such as the 50 μ wide slits 2 and 5, gives similar line widths as shown in figure 19. Interestingly for GI1, GI2 and GI3 changing slit changes the measured line FWHM as given in figure 21 while the change is not so large for GI4 where the difference as predicted from the data of figure 17 is just outside the error bars shown in figure 21. For GI1 and GI2 the measured FWHM agree with predictions while those for GI3 and GI4 are up to 50% higher. However, considering the spread of results obtained for any detector and the difficulties of identifying and allowing for the fixed patterning the agreement of the theory and experiment can be considered satisfactory.

6.2 NIS

Although there was no fixed patterning problem for the NIS, both the number of lines available for use and the time to do the measurements were limited. In the analysis care was taken to avoid saturated lines and data taken with the calibration source misaligned. The results are given in table 6. Within the uncertainties there appears to be no variation in the FWHM across the NI detector and the limited data for NI2 indicate that the FWHM for both channels are the same.

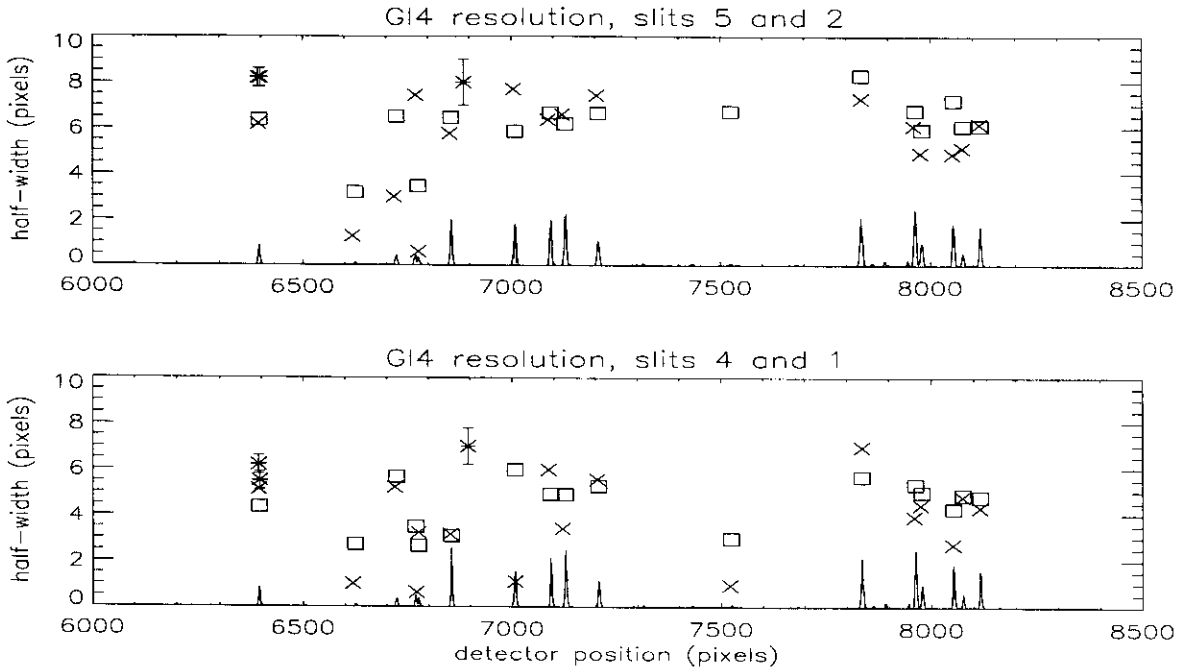

Figure 19: The measured line width (FWHM) for detector GI4. On the upper panel squares represent results using slit 5 and crosses slit 2, on the lower panel slit 4 and 1 respectively. The asterisks for the line at the lowest point are repeated measurements for this line. The point with error bars is the result of measurements at different aperture positions for the same line.

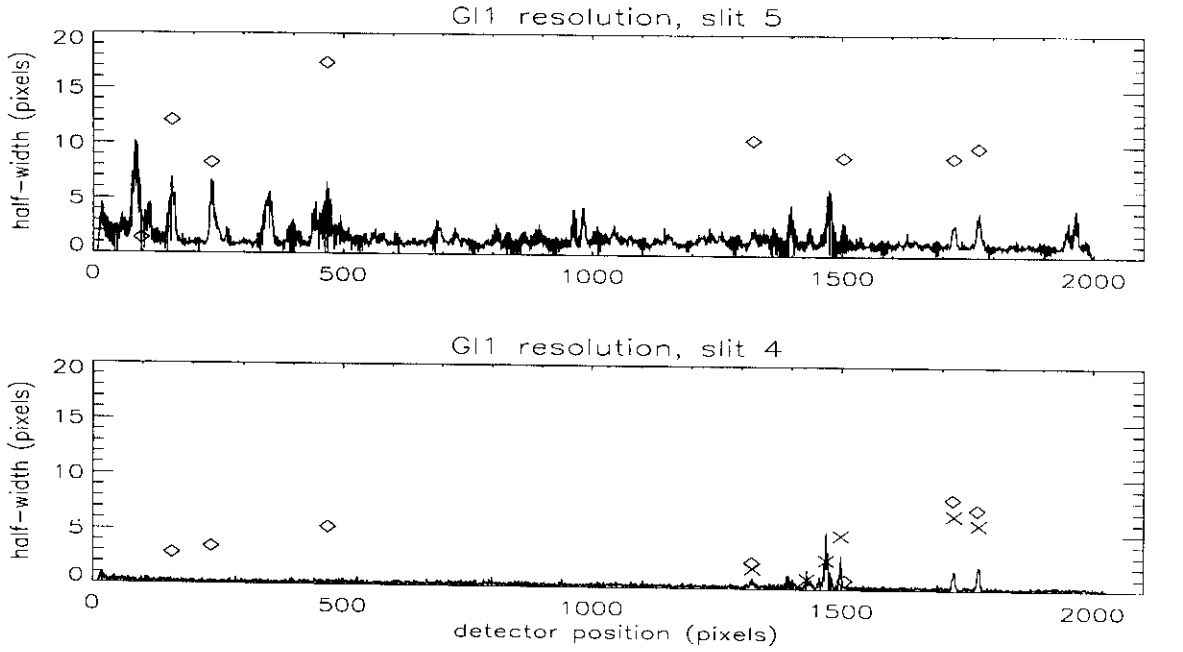

Figure 20: The measured line width (FWHM) for detector GI1. The crosses show measurements using argon lines and the diamonds neon lines.

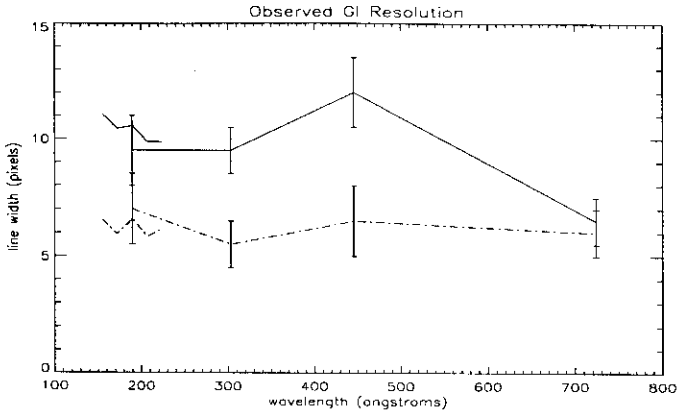

Figure 21: The solid and broken lines (with error bars) denote the mean resolution for the 50 μm and 25 μm slits respectively for each of the GI detectors. Superimposed are the expected FWHM for detector 1, shown as lines without error bars.

Slit, width	Detector NI1			Detector NI2	
	361.0 Å	362.0 Å	379.3 Å	537.0 Å	584.3 Å
6, 1125 μ		48.0±3.0	44.0±4.0	45.0±5.0	
5, 50 μ	3.7±0.5	3.7±0.5		3.7±0.2	
4, 25 μ	3.3±0.5	3.3±0.5	3.6±0.5	3.2±0.2	
3, 100 μ	5.0±0.5	4.8±0.5	5.0±0.5	5.2±0.2	
2, 50 μ	3.9±0.5	3.9±0.5	4.0±0.5	3.7±0.2	
1, 25 μ	3.0±1.0		3.7±0.5	2.8±0.3	3.2±0.5

Table 6: Measured FWHM in pixels for the NI detectors.

For slits 2 and 5 i.e. of the same width but different lengths, the weighted mean of the results is 3.74±0.12 pixels. Similarly for slits 1 and 4 the widths agree within the uncertainties at a particular wavelength. For this latter pair the seven measurements have a weighted mean of 3.20±0.13 and the largest and smallest measurements do not agree within their error bars although they each overlap with the other measurements. Doubling the slit width from 25 μ to 50 μ changes the width only from 3.20 to 3.74 pixels and from 50 μ to 100 μ from 3.74 to 5.11. This is consistent with the detector being slightly offset from the optimal focus position. Considered in wavelength units the measured FWHM for NI1 is 0.25±0.02 Å and for NI2 is 0.36±0.02 Å, that for the NI1 being smaller as it has a more finely ruled grating.

7 Wavelength calibration

7.1 GIS wavelength calibration

For the GI detectors the wavelength calibration as well as depending on the distance from the grating and the offset from the Rowland circle, also depends on the set-up of the detector itself. The changes in wavelength calibration depending on the detector set-up can be evaluated using

the LUT. Such changes do not effect the ends of the detectors so the wavelength ranges remain unaltered. Repeats of a measurement using different LUT start parameters showed changes of up to 40 pixels in line position except as expected near the detector ends. The wavelength calibration is therefore adjusted depending on which LUT start parameter is used. Thus there is a need to establish and maintain a good LUT for a CDS observation.

A small shift is found in the pixel position for the same lines observed using different slits. The results for the GI detectors are given in table 7. For GI4 the large shifts in measured positions between slits 2 and 3 and between slits 5 and 6 are due to the differences in LUT used for the data sets. Apart from this the largest difference is 5 pixels between slits 3 and 4 which are a factor 4 different in width.

Slit, width	Centroid	Shift	Centroid	Shift	Centroid	Shift	Centroid	Shift
1, 25 μm					6370.4		7056.3	
2, 50 μm	2785.8		2968.1		6370.3	-0.1	7056.2	-0.1
3, 100 μm	2785.7	-0.1	2968.7	0.6	6390.5	20.1	7089.6	33.4
4, 25 μm	2790.6	4.9	2973.7	5.0	6394.6	4.1	7092.8	3.2
5, 50 μm	2792.1	1.5	2974.9	1.2	6395.2	0.6	7094.1	1.3
6, 1125 μm					6380.8	-14		

Table 7: Variation of position with slit for the GI spectrometer. The shift for slit n is the difference in position between slit n and slit n-1 data. Lines with pixels around 3000 were observed with detector GI2 and the others with GI4.

The position of the centroid of a line as the narrow source beam was scanned across the GI aperture was found to vary. The results of scans at two different positions for a line observed with detector GI4 are given in figure 22. The measurements agree well with the predictions from the CodeV calculations as given in figure 11, the difference in sign of the shift resulting from the use of absolute pixel number in figure 22. The results for both positions have the same overall shape and the offset between them is attributed to a slight difference in alignment for position G4 compared to that for G2. The data for position G2 correspond to a well aligned on-axis measurement as described in the aperture scan section earlier. The mean position is at aperture point +10 mm where the beam was initially aligned. Wavelength calibrations taken at such points should have the least uncertainty from this movement with aperture position. The combination of data from scans such as shown in figure 22 but with different lines for three of the GI detectors results is shown in figure 23. The results show an asymmetric variation in the shift across each of the detectors and is smallest at the long wavelength end of each detector. The centroid of an observed line was found to vary with scan mirror position at a rate of 0.063 ± 0.004 measured over 80 steps. Time did not permit a study of this over the wavelength range of each GI detector.

In determining the GIS wavelength calibrations the data used were chosen to minimise the effects of the difficulties outlined above. In short the best aligned on-axis positions were selected and, fortunately, only two LUTs had been used. A comparison of desired and expected wavelength ranges for each of the four GI detectors is given in table 8. All the wavelength ranges are slightly to shorter wavelengths than desired. The differences are most probably due to a common effect when building and focusing the spectrometer. The differences in no way change the scientific capability of the GIS. Examination of residuals from a linear fit to the wavelength calibration data showed that a quadratic fit would be better. As the LUTs will change with time, depending both on the

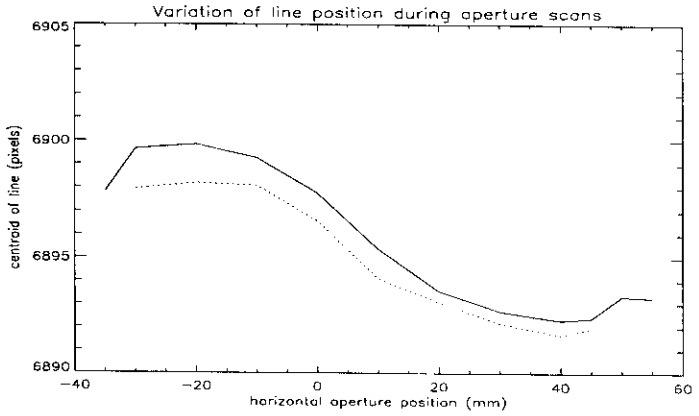

Figure 22: Graph of the centroid position of an isolated line in detector GI4 for a scan of the calibration source across the aperture. The solid line is for an aperture scan at position G2 and the dotted line is for a scan at G4. Note that one pixel is approximately 0.06 Å.

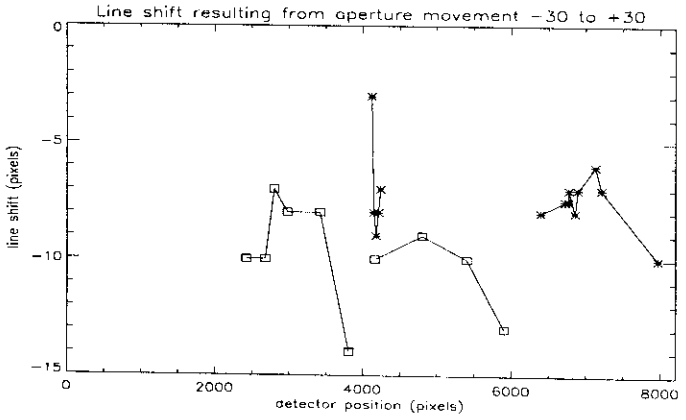

Figure 23: The variation along the detectors of the line-shift caused by moving 60 mm across the central GI aperture. The squares and asterisks are results from measurements of neon and argon lines respectively. A small difference in alignment may be causing a shift between the two data sets.

history of usage and also of the intensities from the particular solar feature being observed, the fits will change. For any particular observation the fit required will be included with the data.

Detector	Slit	LUT	Desired range/Å	Observed Range/Å
GI1	5	3.1	155 - 224	151.95 - 221.83
GI2	5	3.1	261 - 346	256.28 - 339.57
GI3	5	4.1	396 - 495	393.07 - 492.81
GI4	5	4.1	662 - 786	656.89 - 785.24
GI4	4	4.1	662 - 786	656.88 - 785.13
GI4	3	4.1	662 - 786	656.50 - 784.64
GI4	2	4.1	662 - 786	656.54 - 784.70
GI4	1	4.1	662 - 786	656.55 - 784.66
GI4	4	3.1	662 - 786	657.28 - 784.84
GI4	2	3.1	662 - 786	656.63 - 783.59

Table 8: Comparison between wavelength ranges desired for the GIS and those found from the wavelength calibration. Error bars because of possible deviation from on-axis alignment are estimated to range from about 0.05 Å for GI1 to 0.15 Å for GI4.

7.2 NIS wavelength calibration

For the NIS wavelength calibration the problems encountered during the GIS calibration must be addressed, namely the dependence of the calibration on the slit used, the position of the source beam in the NI aperture and the scan mirror position.

The variation in the position of the centroid of a line with slit for the NIS is given in table 9. The uncertainties in the measured shifts are about ±0.4 pixel for slits 1 to 5 and ±2 for slit 6. The largest shift is 3±2 pixels. The data are consistent between NI1 and NI2. Ignoring the wide low resolution slit 6, the pixel shifts between any pair of slits is less than 1.3 pixels.

	NI1		NI1		NI1		NI2	
Slit, width	Centroid	Shift	Centroid	Shift	Centroid	Shift	Centroid	Shift
1, 25 μm	763.0				1017.2		201.0	
2, 50 μm	763.5	0.5	777.5		1017.4	0.2	201.4	0.4
3, 100 μm	763.5	0.0	778.0	0.5	1017.5	0.1	201.3	-0.1
4, 25 μm	764.7	1.2	779.3	1.3	1018.8	1.3	202.5	1.2
5, 50 μm	765.2	1.3	780.0	0.7			203.0	0.5
6, 1125 μm					1020.0		206.0	3.0

Table 9: Variation of line centroid position with slit for the NIS. The shift for slit n is the difference in position between slit n and slit n-1 data.

Considering the shift of line centroid as the source is scanned across the aperture, the scan at the position N3, which was found to be well-aligned at the on-axis position, revealed a shift of 2.1±0.3 pixels as the beam moved from horizontal aperture position 30 to position 70 mm. This

corresponds to a change in angle of incidence of about 14 arc-sec while as described earlier the scanning mechanism was measured as being good to 10 arc-sec over the aperture scanning range. The extra shift may be due to the actual shift in the light path near the edges of the aperture.

For the shift in line centroid with scan mirror position only one pair of measurements with the wide slit 6 was taken, for a mirror position increase of 20 steps. The image of the source clearly moves across the position of the slit but the boundary of the slit image can be clearly seen and this does not move. It should be remembered that when the source is not centred on the slit, the resultant lines appear shifted.

As in the GIS wavelength calibrations the data used for the NI calibration were chosen to minimise the effects of the difficulties outlined above. A comparison of desired and expected wavelength ranges for both the NI detectors is given in table 10. The ranges are in fact for the pixel range 2 to 1021 because two pixels at either end of the range were invalid. The uncertainties are less than those for the GIS since the shift with aperture position was less. As for the GIS all the wavelength ranges are slightly to shorter wavelengths than desired. Again the differences are most probably due to a common effect when building and focusing the spectrometer. The differences in no way change the scientific capability of the NIS. From the limited wavelength range of lines available from the source a linear fit for the pixel to wavelength calibration was found adequate. However, in-flight measurements with many more lines indicate that a quadratic fit is in fact a better approximation.

	Position		Range/Å	
	Aperture	Scan mirr	Desired	Observed
NI1	(25,10)	128	310 – 380	305.5 – 379.6
NI2	(-48,-10)	144	517 – 633	513.2 – 632.9

Table 10: The NIS wavelength calibration obtained for slit 5.

8 Sensitivity

The responsivity calibration of CDS can be obtained by comparing the counts from CDS when illuminated by the calibration source whose output had been measured against a primary radiation standard before and after the CDS calibration, taking account of polarisation effects.

8.1 Polarisation

Although the hollow cathode discharge lamp emits unpolarised radiation the collimating telescope polarises the output beam. The CDS instrument is also sensitive to the polarisation of the radiation observed. However, the orientation of the source and CDS was such that the CDS sensitivity was maximum to the polarisation that the source minimised and for the polarisation that the source maximised, CDS had minimum sensitivity. This 'cross polarisation sensitivity' effect meant that in fact polarisation effects were minimised in the calibration.

The total source flux can be written

$$I_{source} = I_{||} + I_{\perp} \tag{1}$$

where $I_{||}$ and $I_{\perp}$ are the source fluxes in the parallel (p) and perpendicular (s) polarisations respectively.

The flux measured by CDS is

$$I_{obs} = S_{||} I_{||} + S_{\perp} I_{\perp} \tag{2}$$

where $S_{||}$ is the CDS sensitivity to the parallel polarisation and $S_{\perp}$ is the CDS sensitivity to perpendicular polarisation where $||$ and $\perp$ are taken with respect to the dispersion planes of the spectrometer (NIS or GIS). The CDS unpolarised sensitivity is given by

$$S = S_{||} + S_{\perp} \tag{3}$$

The observed flux can be then be re-written as

$$\frac{I_{obs}}{I_{source}} = fS \tag{4}$$

where

$$f = \frac{S_{||} I_{||}}{S I_{source}} + \frac{S_{\perp} I_{\perp}}{S I_{source}} \tag{5}$$

is the polarisation correction to be applied. As the product fS is measured the need is to evaluate f to obtain S.

In deriving f it is convenient to consider the collimating telescope and the CDS telescope and scan mirror together as they are common to both the grazing incidence and normal incidence spectrometers.

The polarisation response of these optical elements was calculated using the computer progam of Browning, Kent and Richards (1997). This is a recursive thin film layers code modified to provide calculations for multilayer x-ray optics. As input it requires the wavelength range of interest, the incident angle of the radiation as well as the optical constants for the materials used which are shown in figure 24.

The collimating source Wolter II telescope was modelled as two flat glass mirrors (primary and secondary) at the mean incident angles. The calculated calibration source polarisations are plotted in figure 25. The source polarisation ratio $I_{||}/I_{source}$ needed in the calculation of the factor f can be expressed as follows

$$\frac{I_{||}}{I_{source}} = \frac{R_{coll.primary}^{s-polarisation} R_{coll.secondary}^{s-polarisation}}{R_{coll.primary}^{s-polarisation} R_{coll.secondary}^{s-polarisation} + R_{coll.primary}^{p-polarisation} R_{coll.secondary}^{p-polarisation}} \tag{6}$$

where the various R factors are given in figure 25. The ratio $I_{\perp}/I_{source}$ can be evaluated in a similar manner.

The CDS telescope and scan mirror grazing angles are crossed and the polarisation sensitivities of the combination of telescope and scan mirror $S_{||}^{TM}$ and $S_{\perp}^{TM}$ can be expressed as follows

$$S_{||}^{TM} = R_{primary}^{p-polarisation} R_{secondary}^{p-polarisation} R_{scanmirror}^{s-polarisation} \tag{7}$$

$$S_{\perp}^{TM} = R_{primary}^{s-polarisation} R_{secondary}^{s-polarisation} R_{scanmirror}^{p-polarisation} \tag{8}$$

In calculating these polarisation sensitivities the primary and secondary sections of the CDS telescope were taken as flat mirrors coated with the specified materials (500 Å of Au on 100 Å of Cu)

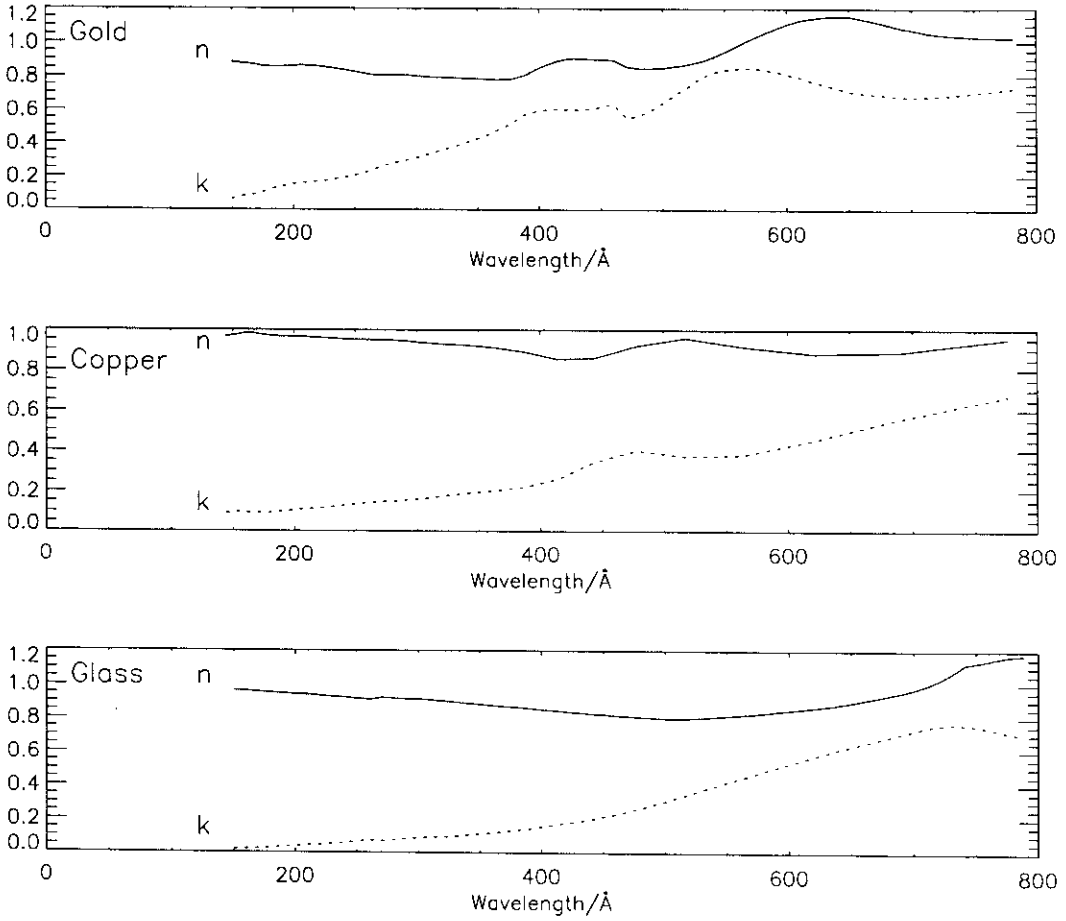

Figure 24: Optical constants, taken from Lynch and Hunter (1985), for polarisation calculations

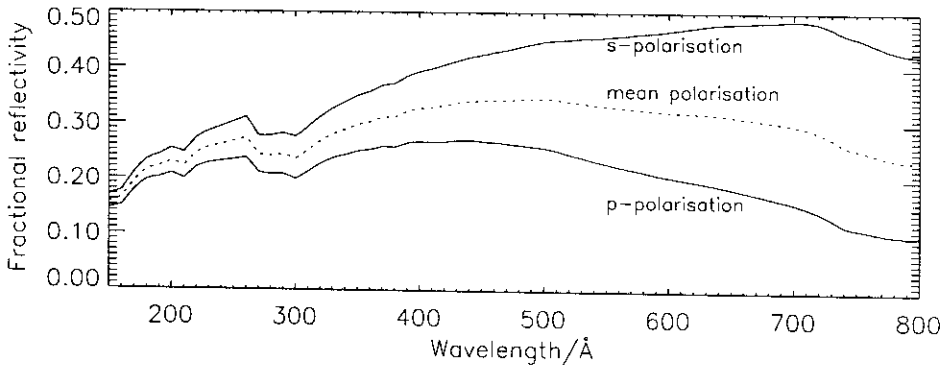

Figure 25: The calibration source polarisation reflectivities

on the glass substrate. The radiation is incident at grazing angles from 12.6° to 17.3° and 11.1° to 18.4° on the primary and secondary sections respectively and the mean values (75.05° and 75.25°) were used in the polarisation calculation. The scan mirror was modelled with the same coatings as the telescope and taken as a flat mirror at its central on-axis position, i.e. at a grazing incidence angle of 5°. The polarisation sensitivities of the combination of the CDS telescope and scan mirror are shown in figure 26.

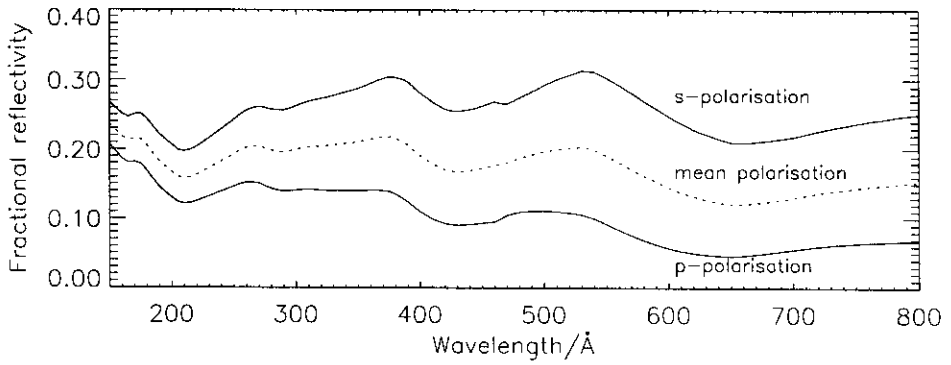

Figure 26: The CDS telescope and scan mirror polarisation reflectivities

To obtain f for NI1 and NI2 the polarisation sensitivities of the appropriate grating with radiation incident at between 7° and 9° and of the VDS detector must be included in the calculation. Although Samson (1967) points out that no appreciable polarisation has been reported using normal incidence monochromators with angle of incidence less that 10°, the gratings were modelled as mirrors at 7.9°, the mean angle of incidence of the radiation. The response of microchannel plates to polarisation has been studied experimentally by McConkey, Crouch and Tomc (1982) and Tomc et al. (1984). For the NIS with the radiation angles of incidence of 15° on the pores of the MCP their work gives $S_{||}/S = 0.585$ and $S_{\perp}/S = 0.415$ at 584 Å. As the sensitivities are only reported at one wavelength they are assumed to be constant with wavelength in the present calculation.

The polarisation sensitivities of the NIS, including all optical elements and the detector, $S_{||}^{NI}$ and $S_{\perp}^{NI}$ can be expressed as follows

$$S_{||}^{NI} = R_{primary}^{p-polarisation} R_{secondary}^{p-polarisation} R_{scanmirror}^{s-polarisation} R_{grating}^{s-polarisation} \left(\frac{S_{||}}{S_{detector}}\right) \tag{9}$$

$$S_{\perp}^{NI} = R_{primary}^{s-polarisation} R_{secondary}^{s-polarisation} R_{scanmirror}^{p-polarisation} R_{grating}^{p-polarisation} \left(\frac{S_{\perp}}{S_{detector}}\right) \tag{10}$$

The factors $S_{||}^{NI}$ and $S_{\perp}^{NI}$ are graphed in figure 27. The factor f for the NI1 and NI2 wavelength ranges evaluated using the calculated polarisation sensitivities is given in figure 28.

The factor f was also evaluated for the GIS. Here the angle of incidence on the grating is 84.75° and the grating was modelled as a plane gold reflector at the incidence angle minus the blaze angle of 5.42° i.e. 73.91°. The angles of incidence of the radiation on to the detectors range from 66.5° to 76.8° while the angle from the pores to the normal is 13°, resulting in the angles of incidence of the radiation to the pores being from 53.5° to 63.8°. The results of Tomc et al. (1984) only extend up to 40° at 584 Å and this is used for our estimate, giving $S_{||}/S = 0.570$ and $S_{\perp}/S = 0.430$. The polarisation sensitivities of the GIS, including all optical elements and the detectors, $S_{||}^{GI}$ and $S_{\perp}^{GI}$

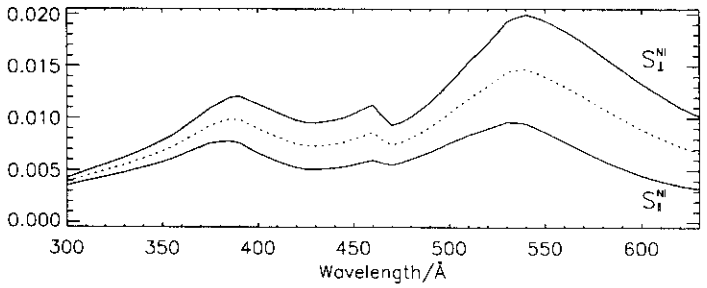

Figure 27: The factors $S_{\parallel}^{NI}$ and $S_{\perp}^{NI}$ for the NI1 and NI2 wavelength ranges

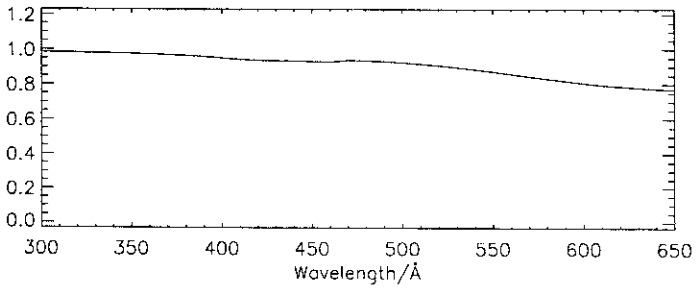

Figure 28: The factor f for the NI1 and NI2 wavelength ranges

can be calculated using expressions analogous to equations 9 and 10 and are plotted in figure 29. The factor f for the GIS wavelength ranges evaluated using the calculated polarisation sensitivities is given in figure 30.

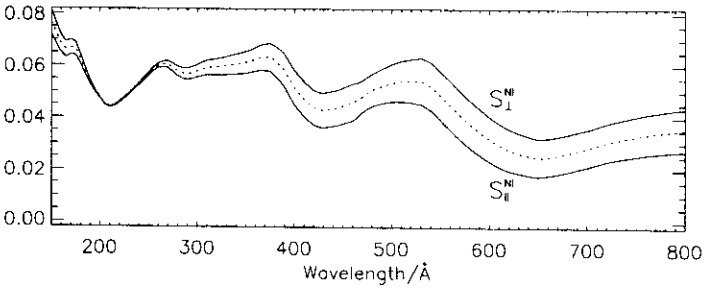

Figure 29: The factors $S_{\parallel}^{GI}$ and $S_{\perp}^{GI}$ for the GIS wavelength ranges

8.2 Calculated sensitivities

To derive the estimated sensitivities for the normal incidence spectrometer, the mean reflectivities of the telescope and scan mirror obtained in the polarisation calculation were multiplied by the normal incidence grating sensitivities as measured by Thomas (1994) and detector quantum efficiencies as measured by Thompson et al. (1992). The various efficiencies and the resulting estimated first order

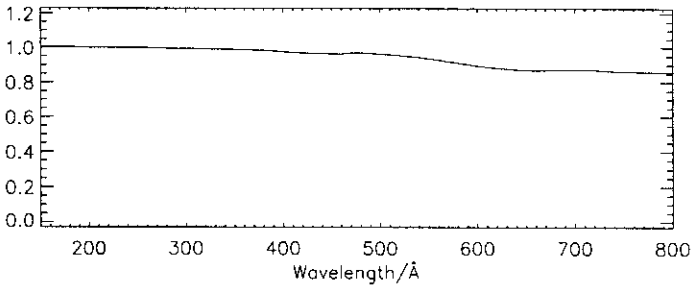

Figure 30: The factor f for the GIS wavelength ranges

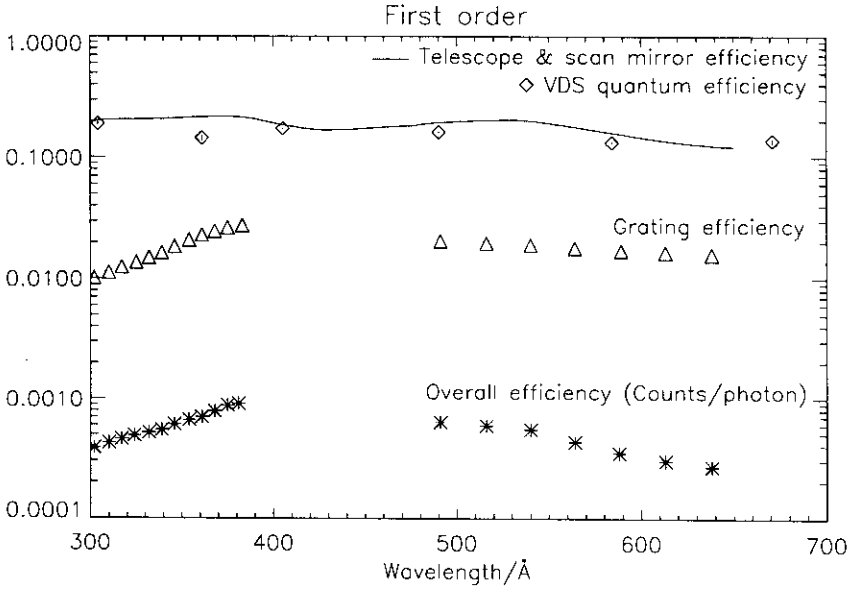

Figure 31: The telescope and scan mirror, grating and detector efficiencies and the expected overall efficiency of the NI spectrometer as a function of wavelength.

sensitivities for both NI1 and NI2 are shown in figure 31. The second order efficiencies, shown in figure 32, were evaluated using the same telescope and scan mirror data, the second order grating efficiencies as measured by Thomas (1994) and assuming the quantum efficiency of the detector to be the value at 304 Å.

To derive the estimated sensitivities for the grazing incidence spectrometer, the mean reflectivities of the telescope and scan mirror and grating obtained in the polarisation calculation were multiplied together along with the estimated quantum efficiency of the GIS MCP. The estimated quantum efficiency was linearly interpolated between the values of 2.6%, 3.4%, 4.1% and 2.2% at 150 Å, 303 Å, 584 Å and 920 Å respectively following the review by Breeveld (1995). The various efficiencies and resulting sensitivities for the GIS wavebands are shown in figure 33.

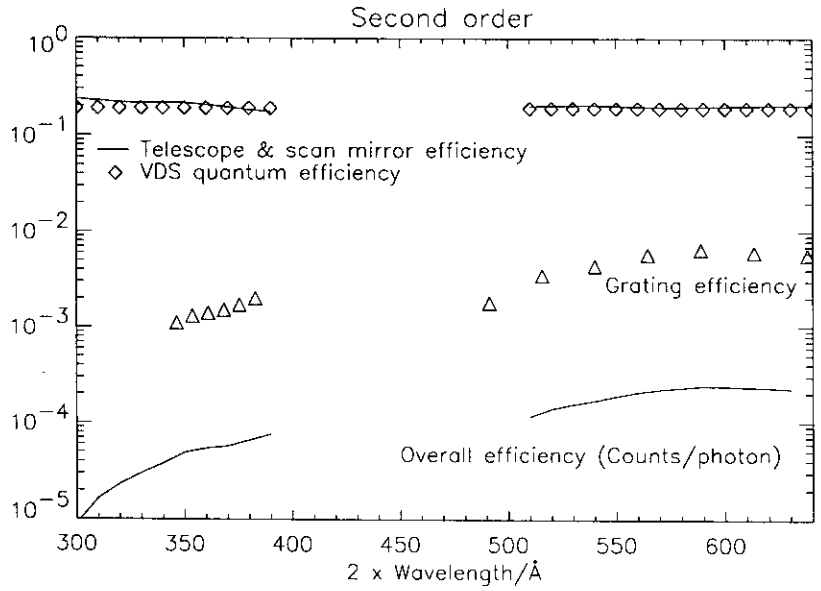

Figure 32: The telescope and scan mirror, grating and detector efficiencies and the expected overall efficiency of the NI spectrometer in second order as a function of wavelength.

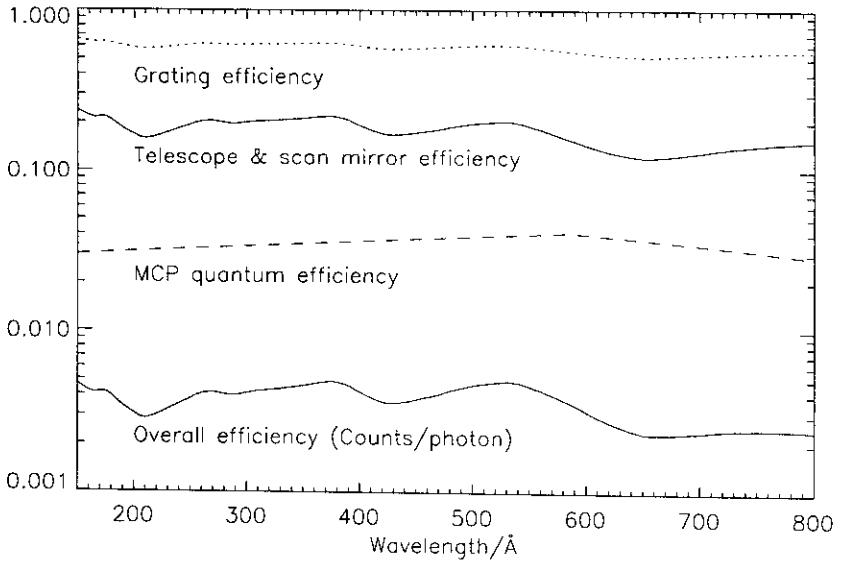

Figure 33: The telescope and scan mirror, grating and detector efficiencies and the expected overall efficiency of the GI spectrometer as a function of wavelength.

8.3 The NI sensitivity

8.3.1 NI calibration measurements

Changing slit changes the measured intensity. NI1 spectra using neon lines were used to provide measured ratios to check against the geometrical ratios, recalling that the source beam is 0.9 mm along the slit. The results, given in table 11, are much as expected.

Slit	Slit size μm × μm	Observed ratio	Expected ratio
6	1125×3000	1	1
5	50×3000	$(5.3\pm0.1)\times10^{-2}$	5.3×10^{-2}
4	25×3000	$(3.0\pm0.1)\times10^{-2}$	2.7×10^{-2}
3	100×625	$(1.00\pm0.02)\times10^{-1}$	1.04×10^{-1}
2	50×50	$(5\pm1)\times10^{-3}$	4×10^{-3}
1	25×25	$(1.0\pm0.3)\times10^{-3}$	1×10^{-3}

Table 11: Ratios of measured count rates for the same lines observed with different slits.

It had been anticipated that the responsivity calibration would be done using the largest slit, 6, to maximise the observed count rates. The profile of the source was determined using that slit, see section 4. It is calculated using the NI image data that the maximum proportion of the source beam which could pass through the slit is 74±4%. Examination of NI images of lines, as shown in figure 34, revealed a small-scale spatial non-uniformity with a scale of a few pixels which would not cause problems when using slit 6.

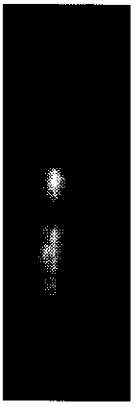

Figure 34: Image of a neon line taken with NI1 using slit 4.

However, because of the limited time available data taken using slits other than slit 6 have had to be analysed. The structure in the source beam means that for imperfect or slightly defocused optics then a 'finger-print' of the source structure could remain in the CDS telescope image plane and such data could be more sensitive to misalignment than anticipated due to the possibility of bright points within the source not being aligned with the entrance slit in use.

The calibration apparatus had been assembled on the understanding that holding alignment to better than ±10 arc-sec would be adequate when using slit 6 alone with an unstructured source

beam. The sensitivity of the calibration to the alignment of the source in pitch and yaw (source to CDS optic axis) was not explicitly measured because of time constraints. The information is partially available from the scan mirror scan described in section 4 and plotted in figure 4. This gives the sensitivity to yaw for light integrated along the spatial direction. Since the scan mirror scan intensity falls by no more than 10% of the peak value within ±10 arc-sec of the on-axis position, the target stability in yaw is adequate. Figure 35 shows the total radiation intensity recorded in the GI2 waveband as the 4 arc-sec by 4 arcsec slit was scanned in pitch through the stationary, focused image of the calibration source. These data can be used to estimate the sensitivity to misalignment in pitch for this particular source position. Unlike the yaw case, the radiation distribution is not symmetrical about the mid position so that misalignment in pitch is more severe as the intensity can fall to 80% of its peak value over a range of ± 10 arc-sec. Thus in evaluating responsivity calibrations care must be taken to use only data with good alignment, especially in pitch. Both scans show that in fact the 'finger-print' from source beam non-uniformities mentioned above does not cause too much trouble.

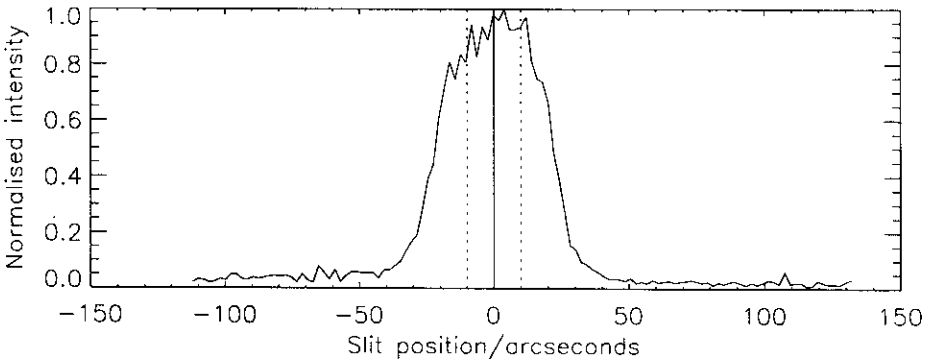

Figure 35: Results from a slit scan using the 4 arc-sec by 4 arc-sec slit

The available data for the NI1 spectrometer are for the neon line groups as listed in table 2. In most cases these lines are rather faint and dominated by a large thermal signal so that a background dark image needs to be subtracted before the spectrum is revealed. The lack of visibility of the data was misunderstood at the time of the actual calibration and in order to bring the spectrum to a level visible in 100 s the gain on the detector was maximised. This meant that many subsequent observations were saturated, primarily in the NI2 channel. The He 584 Å data at integration periods of longer than a few seconds were particularly affected and a few of the wide slit 6 measurements with argon. Again this was not obvious until after the calibration was complete and many of the resulting spectra cannot be used. Fortunately the short duration He 584 Å observations are fine.

In the case of NI2 the data are more abundant consisting of lines from helium and argon, as listed in table 2. The set of well aligned He I observations gives measurements at 584 Å and 537 Å in slits 6, 5, 4 and 3. The Ar II lines in the bands 567-592 Å and 592 to 622 Å are not on the original list of calibration lines as they are not well isolated lines but nevertheless are available with broad band calibrated intensities from the CDS source. In table 2 the CDS source photon fluxes in the Ar II 542.9 - 543.4 Å, 547.5 Å and 583.4 Å lines were estimated from the intensities of the lines from the source used to obtain the spectral sensitivity of the SOHO SUMER instrument (Hollandt et al. 1996b). Inferring CDS source line intensities from SUMER source intensities can be dangerous because of the differing optics and operating conditions. The SUMER source uses normal incidence

optics and operates at a current approximately half of that used in the CDS source. However, after several comparisons it appears that these caveats apply mostly to the He I 584.3 Å and 537.0 Å lines. For other lines examined a constant ratio of 3.6 ± 0.5 (±14%) between the two sources applies.

The best data for sensitivity measurements are the wide slit 6 observations particularly the bright He I 537 Å and 584 Å lines, which because of their high intensity have minimum uncertainties due to counting statistics and background subtraction. Also the wide slit observations reduce any uncertainty caused by non-optimum alignment. Additionally there is the benefit that only relatively well aligned observations can be selected, as the correctness can be verified from the source spot image in the VDS detector.

8.3.2 Analysis of calibration data

As discussed in section 5.1.1 and in particular figure 12 sensitivity measurements made using a narrow beam source near the centre of the aperture will need to be corrected for full aperture illumination and the correction factor 1.04 has been applied to the results for both NI1 and NI2. Allowance has been made for the proportion of incident flux entering the aperture and the effects of polarisation. The corresponding uncertainties have also been included. Neither the uncertainty in the source calibration nor that needed to allow for change of detector high voltage have been included. The inclusion of these uncertainties depends on the particular application of the responsivity calibration as discussed in section 9.

In analysing the NI2 data, corrections were made for non-linearity at high count rates (1%) and for a small difference between the actual and recorded exposure times for very short (1 second) exposures (5%).

8.3.3 NI2 sensitivity results

First order

The measured and expected sensitivities for NI2 are given in figure 36. Note the differences between the measurements where their wavelengths overlap. We propose that the He I data (537.0 Å and 584.0 Å) are correct for the reasons outlined previously, namely that these lines have high intensities minimising uncertainty due to counting statistics and background subtraction. The use of the largest slit (6) minimises the uncertainty caused by misalignment as it is possible to observe the source spot image using this slit and select only well aligned data. Indeed, there are non-aligned slit 6 data giving results like those obtained using the smaller slits. It is assumed that the data for slits other than 6 were taken with the source misaligned, misalignment not being uncommon in the data. There is no reason to suspect that the slit 6 data are in error. A possible source of error is the original source calibration. However, this calibration included several cross checks and independent measurements, and is a very unlikely source of error. To normalise the Ar II data to the He I slit 6 results, a factor 1.7, the difference between the He I 584 Å and the Ar II 567 - 592 Å results, is applied. The comparison of the He I and normalised Ar II data to the predicted sensitivity is given in figure 37. The correspondence between the measured and predicted data is reasonably convincing. As both the He I 537.0 Å and 584.3 Å lines were measured simultaneously it is not possible to prefer one or other of the results. Therefore, the calibration for NI2 is taken as the mean of these results at their mean wavelength, and the slope of the calibration is taken as

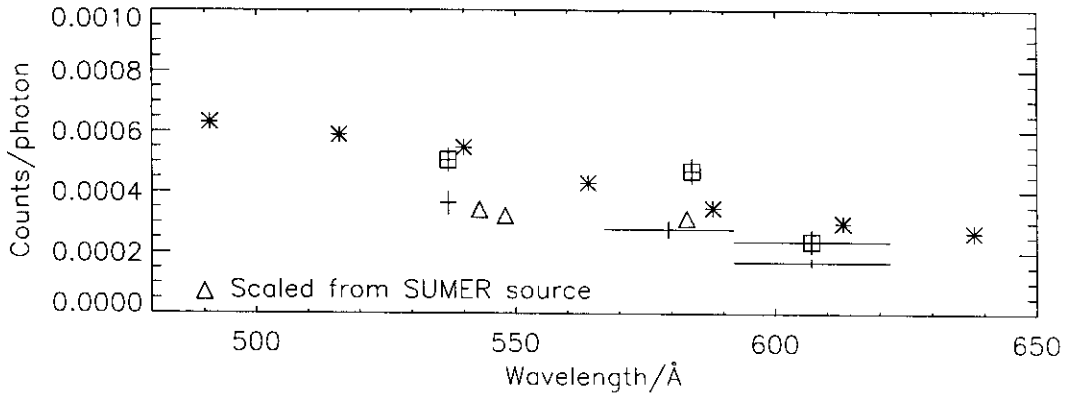

Figure 36: Comparison of measured and expected sensitivities for NI2. The expected sensitivities (see figure 31) are denoted by asterisks. The slit 6 data are given by □. The other data were taken using different slits. The lines used can be identified from their wavelengths and data in table 2.

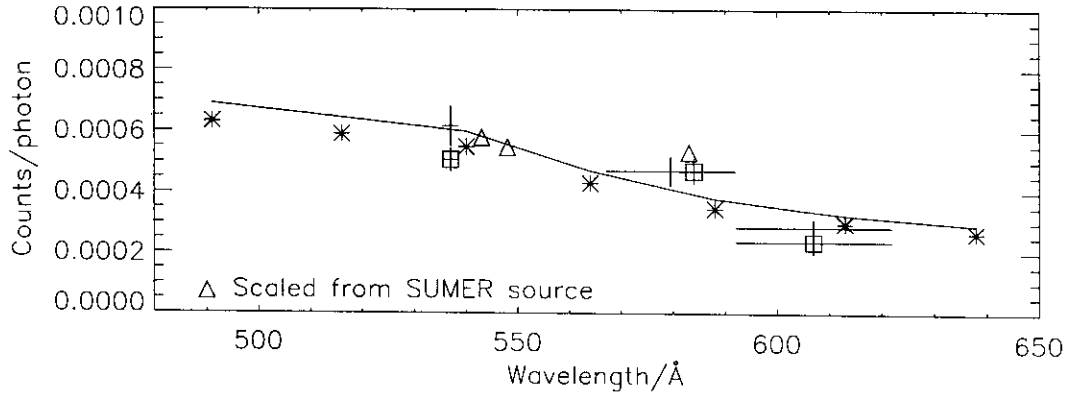

Figure 37: Comparison of normalised and expected sensitivities for NI2. The symbols are as for figure 36. The continuous line shows the adopted sensitivity.

that given by the estimated sensitivity. The best estimate of the NI2 sensitivity is given in table 12. The uncertainty in the He I slit 6 data is estimated at ±8% and ±9%. The uncertainty in the adopted calibration is taken as ±23% so that the He I data points lie within the error bars of the adopted calibration and that allowance is made for the uncertainty in the factor f.

Second order

When using the hollow cathode with helium buffer gas to measure the NI2 sensitivity as well as detecting the calibrated He I lines in first order, the calibrated He II 303.8 Å line was seen in second order. When observing the He I lines the exposure time was kept usually to around 1 s to avoid saturation. Under these conditions the He II line, although observable, had poor signal to noise ratio. Fortunately, one exposure of 15 s was taken. This gave a clear and obvious slit 6 measurement, yielding $(1.32\pm0.11)\times10^{-5}$ counts/photon for the sensitivity. This well-aligned measurement is taken as the basis of the second order NI2 calibration. In addition measurements

Wavelength/Å	First order Counts/photon	Second order Counts/photon
513.0	6.49×10^{-4}	6.94×10^{-6}
516.0	6.44×10^{-4}	7.34×10^{-6}
540.0	5.98×10^{-4}	9.54×10^{-6}
564.0	4.70×10^{-4}	1.20×10^{-5}
588.0	3.79×10^{-4}	1.34×10^{-5}
613.0	3.26×10^{-4}	1.31×10^{-5}
633.0	2.99×10^{-4}	1.25×10^{-5}

Table 12: Best estimate of counts per photon for NI2

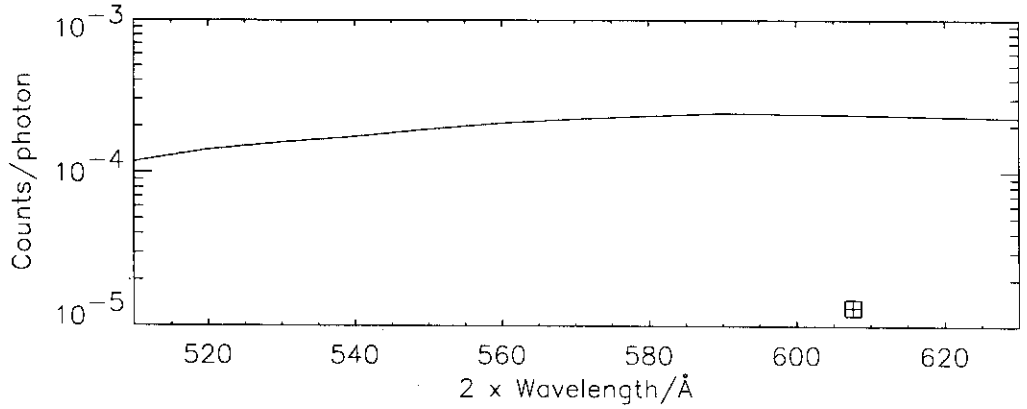

Figure 38: Comparison of measured (□) and expected (continuous line) second order sensitivities for NI2.

of the He II line were also made using slits 3, 4 and 5 where the quality of the alignment cannot be confirmed. Using the measured slit ratios with these data yields a value of $(1.61\pm0.31\times10^{-5})$ for the sensitivity. The uncertainty comes from the mean of the 5 observations which are estimated each to have typically ±10% uncertainty. Figure 38 shows the comparison of measured and expected second order sensitivities for NI2. The discrepancy between the measured and expected sensitivities is discussed with the NI1 sensitivity results. The second order sensitivity is taken as the expected sensitivity divided by 17.9 so that it passes through the measured slit 6 point while retaining its expected slope and is given in table 12. An uncertainty of ±25% is assigned to the second order sensitivity where allowance has been made both for the uncertainty in the measurements and in the calculation of the slope of the expected sensitivity.

8.3.4 NI1 sensitivity results

The comparison of measured and expected sensitivities for NI1 is shown in figure 39. The agreement is not good, the measured sensitivities being much lower than the prediction. Reducing the predicted sensitivity by a factor 11.6 brings the prediction between the measurements in the 312 to 315.5 Å waveband into agreement, as shown in figure 40. The measurement at 379.3 Å is from

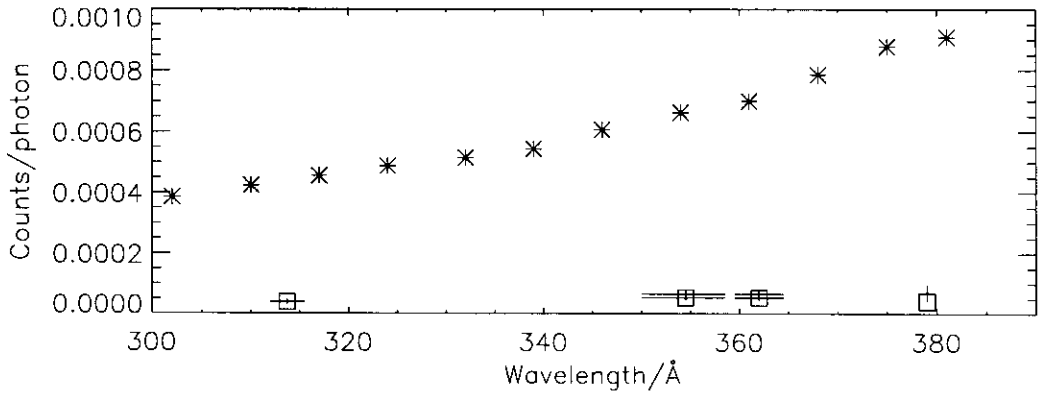

Figure 39: Comparison of measured and expected sensitivities for NI1. The symbols are as for figure 36.

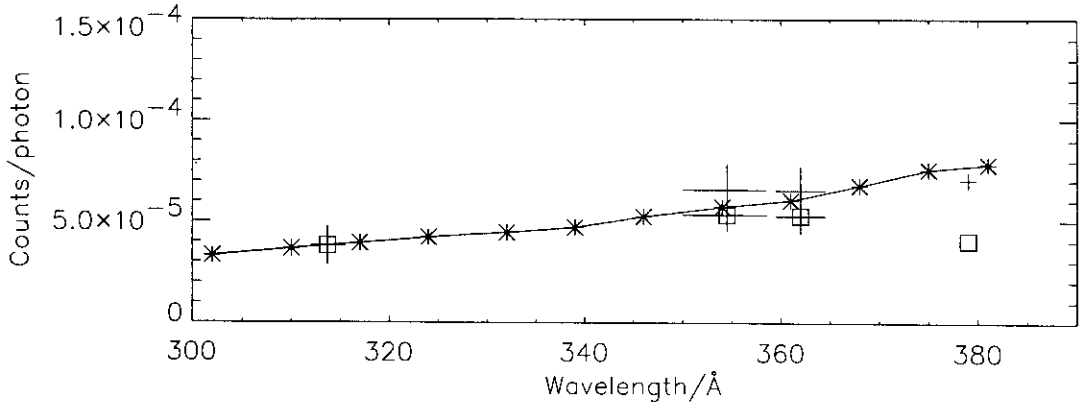

Figure 40: Comparison of measured and scaled expected sensitivities for NI1. The symbols are as for figure 36. The continuous line with asterisks shows the adopted sensitivity.

a slit 6 measurement for a single line. Unfortunately, it is at the edge of the detector and flux is lost, so it only provides a lower limit. The other slit 6 measurements were not of single lines and the images are weak making it difficult to check the alignment. The other measurement at 379.3 Å is also treated with caution. Ignoring the 379.3 Å data, the comparison of scaled and measured data shows that their wavelength dependence is similar.

Thus we have one channel of the normal incidence spectrometer where the measurements and predictions of sensitivity agree for first order while for second order of that channel and first order of the other there are differences of more than a factor of ten. The only differences between the channels are the gratings and areas of the detector used. The grating efficiencies were measured in the same apparatus pre-launch. They went through the instrument build programme together. It is difficult to do something to one but not the other. One possibility is that one was incorrectly installed in the spectrometer. This is ruled out as they each have a unique shape and they were tested in the same orientation as they are flown. Contamination could change the sensitivity. Taking the model and adding a uniform layer of low atomic number material to the surfaces can

Wavelength/Å	Counts/photon
307.0	3.53×10^{-5}
310.0	3.65×10^{-5}
317.0	3.93×10^{-5}
324.0	4.20×10^{-5}
332.0	4.44×10^{-5}
339.0	4.69×10^{-5}
346.0	5.23×10^{-5}
354.0	5.71×10^{-5}
361.0	6.03×10^{-5}
368.0	6.77×10^{-5}
375.0	7.56×10^{-5}
381.0	7.83×10^{-5}

Table 13: Best estimate of counts per photon for NI1

introduce a factor three difference between the NI1 and NI2 responses. This is a poor model of contamination. Furthermore, neither the witness samples that accompanied the optical elements up to integration nor the quartz crystal microbalances subsequently used with the flight model to measure contamination show any evidence for contamination. However, although different areas of the detector are used the common factor between first order in NI1 and second order in NI2 is the overlap of the wavelength ranges, namely 306 - 308 Å and 257×2 - 316×2 Å respectively. If the detector quantum efficiency for these wavelength ranges was too high by between a factor 11 and 19 the major discrepancy would be removed. The possibilities for such a change occuring include mistakes in the original measurements and contamination subsequent to this. The effects of contamination on the detector quantum efficiency are difficult to assess, especially in the present case where it appears that the performance at around 600 Å is not changed while that at around 300 Å is changed by more than a factor of ten. The laboratory results apart from those at 379.3 Å are therefore taken to define the NI1 sensitivity and the scaled expected sensitivity to give the wavelength dependence. Our best estimate of the NI1 sensitivity is given in table 13. The uncertainty in the slit 6 data points ranges is ±15% to ±25%. The factor f lies between 0.98 and 0.96. If this change of 2 to 4% is correct say to ±25% this would imply a difference of 1% in the 4% which can be ignored compared to the error in slit 6 data points. A value of ±25% is taken for the uncertainty in the adopted sensitivity for NI1. The choice for the NI2 second order calibration was made to be consistent with the NI1 first order calibration.

8.4 The GI sensitivity

Considering the source alignment, the aperture scan measurements made with the GI instrument revealed a variation in the maximum count-rate of up to 58% (see table 4). From the measurements it was possible to correct for the proportion of the incident source beam which passed through the slit at each of the positions of the aperture scan. Also some data were rejected as being taken with incorrect source alignment, whereby the counts in the lines in all detectors in use were considerably lower than for data known to be taken with the source correctly aligned.

Slit 6 was designed for use with the NIS and using it with the GIS gave problems with the detectors

giving count rates which approached or exceeded the limits of the detector system count rate capability. Consequently, smaller slits (1, 3 and 5) had to be used for the responsivity calibration, adding the uncertainty associated with the slit ratio measurements. Also, the small-scale variability in the source image as discussed for the NI calibration became significant.

Any data not taken with the correct high voltage or LUT were rejected. In using the GIS detectors as well as allowing correctly for effects such as linearity, deadtime, flat-fielding, ghosting and fixed patterning, gain depression has to be monitored. At high count rates per pore of the MCP, count rate dependent gain depression (CDGD) can cause loss of counts as the reduction in gain means that some events which should have passed the lower-level discriminator (LLD) do not. As the total number of counts observed by the detector increases, long term gain depression (LTGD) must be monitored. LTGD affects the detector globally, because of for example plate ageing, and differentially since any spectrum contains a mix of strong and weak lines which effectively always illuminate the same place on the detector. The HV applied to the detector can be increased or the LLD lowered to compensate, but for the latter the range of adjustment is limited.

The reduction in count rate during the calibration was monitored for each of the four GIS detectors from data taken for different vertical positions on the aperture with slit 6. As the aperture scan analysis showed that the illumination at the various positions was not the same, the results were normalised to correct for this. For detector GI4 the results are shown in figure 41. The normalised count rate declines with time, apart for the data taken for aperture position G2. At this position the count rates were largest (about 50% higher than the others) and the data are affected by CDGD. The drop of about 50% measured for GI4 was also measured for GI3 but was only about 20% for GI1 and GI2, presumably due to lower overall illumination for these two detectors.

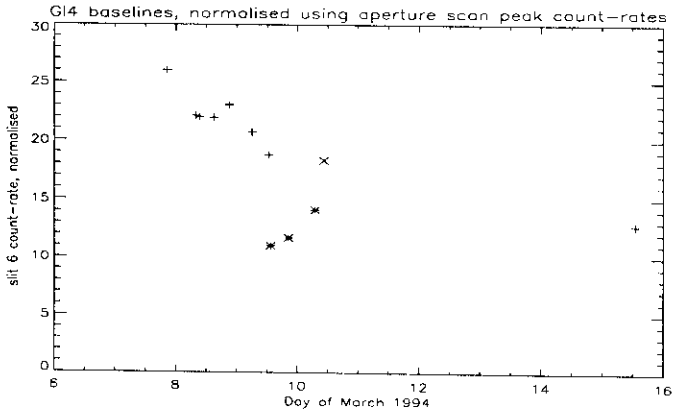

Figure 41: Variation in slit 6 count rates during the calibration, normalised by dividing by the corresponding aperture scan peak count-rate. The symbols *, + and × show data taken at aperture position G2, G3 and G4 respectively. The data at G2 are depressed by CDGD.

The performance of the detectors with time (i.e. LTGD) was monitored by using the electron filaments, by comparing data taken at different times with the same filament and detector settings and assuming that the filament output did not change significantly. This was done twice, once near the start and the other near the end of the calibration period. A gain loss correction curve was derived by averaging the data from each filament and then taking the ratio of the 'end' to 'start' data, setting the mean level to unity. The correction curve for detector GI3 and the source spectrum are shown in figure 42. The dips in the correction curve correlate well with the positions of the spectral lines.

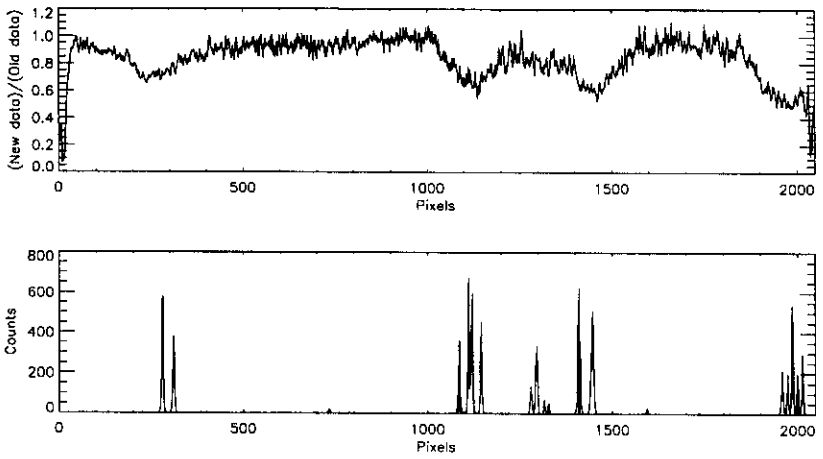

Figure 42: Gain correction curve for detector 3 from the averaging of filament data from early and late times in the calibration. A neon source spectrum is also shown.

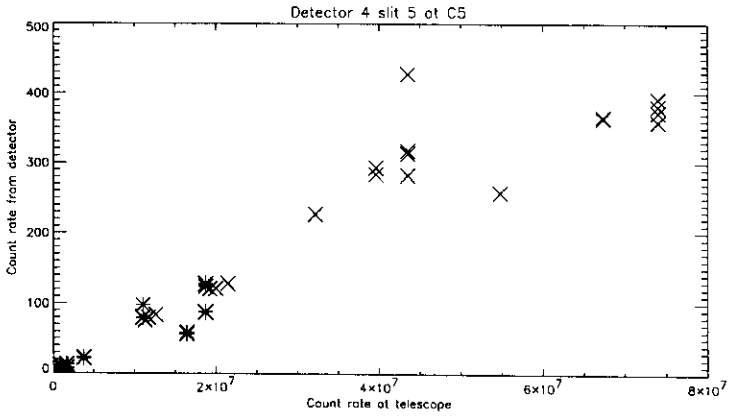

Figure 43: CDGD curves for detector 4, taken with slit 5 at 3.94 kV. The asterisks and crosses indicate data from neon and argon line measurements respectively. Linearity is maintained to about 300 counts/s.

Count rate dependent gain depression had to be corrected for. Although the gain depression for a bright line can be compensated for by increasing the applied high voltage, doing so can mean that less bright lines may then have their pulse heights above the upper level discriminator and so are not recorded properly. Ideally to obtain a CDGD curve, i.e. a plot of count rate output versus count rate input to a detector, the source intensity should be varied and the change in response measured. The calibration source was of fixed intensity. However, the variation in count rate as the source was scanned over the edge of the aperture was used to produce a CDGD correction. Data from different slits were used, corrected to allow for different width slits illuminating different areas of pores on the detector. Measured count rates for known input count rates as measured for detector GI4 at 3.94 kV with slit 5 are shown in figure 43. The maximum linear count rate, i.e. the rate at which the CDGD curves become non-linear, as a function of applied voltage were also determined.

Although the detector dark counts are less than 2 counts/s, background due to scattered light had

to be subtracted for detector 1. The background was estimated by considering line-free regions adjacent to each line and estimating the mean background rate. Correcting for this rate added 30% uncertainty to the uncertainty in the line flux as obtained from Poisson statistics. In considering the uncertainties of the flux measurements, a 10% allowance was taken for LUT corrections, 10% was also allowed for correcting the count rate for aperture position and 10% each for LTGD and CDGD. For slits 1 and 3, mostly 5 measurements for each line were averaged together (only 3 for detector 1) and for slit 5 over 10 measurements were averaged. The results of the calibration are shown for each slit in figure 44, including the uncertainty in the measured slit ratios. For the two lowest wavelength lines in detector 1 the measurements of the same line using both argon and neon as buffer gases in the source have been combined while for detector 4 the measurements using neon and argon lines have been shown independently. For detector 3 the Ne III lines at 488 - 491 Å lie too close to the edge of the detector (see figure 42) and have been omitted from the analysis. In addition the results obtained using the measurements of the Ne II lines at 460.7 - 462.4 Å have also been omitted from the analysis. When using slit 1 the data for this multiplet show strong ghosting for some but not all of the observations, casting doubt on the detector set-up. These are the lines for which the greatest count rates were observed. Thus when using slits 3 and 5 there are additional doubts about the count rates being too high.

The measurements for these three slits have been combined at each wavelength by taking weighted averages and are plotted in figure 44. The uncertainties are around ±25% for detector 1, ±20% for detectors 2, 3. For detector 4 the argon data have uncertainties of ±20% while the neon data have uncertainties of more than ±50%. This greater uncertainty for the neon detector 4 results arises from the large spread in the sensitivities obtained using the different slits, particularly the low values from the slit 1 measurements. In fact the slit 3 and 5 results for detector 4 from neon and argon lines agree within the uncertainties. The argon data for detector 4 are taken to define the calibration. Also plotted with the average data for all three slits is the estimated sensitivity as given in figure 33 divided by a factor of 20. Considering the relative crudeness of the estimate, particularly for the grating and detector efficiencies, and comparison of the estimates and measurements for the NIS where both the grating and detector efficiencies had been measured, the agreement between the measurements and the shape of the curve is satisfactory.

The data defining the calibration are given in table 14. To obtain values for any wavelength for a particular detector it is recommended simply to do a linear interpolation between the data points. Linear extrapolation to extend the wavelength ranges is also suggested apart from the short wavelength end of detector 1 where the value at the edge of the detector should be the same as that at 172.6 Å. In evaluating the results note that the correction of a factor 1.04 discussed in section 5.1.1 to allow for using a narrow beam source near the centre of the aperture instead of full aperture illumination was applied.

9 Application of calibration

In applying the laboratory calibration to observations of the Sun, the change of illumination must be allowed for. The laboratory calibration was done using a small source which had to be mapped over the relevant telescope aperture in order to fill it, while solar illumination fills the aperture. The astigmatism of the grazing incidence spectrometer must be considered for the two cases. Astigmatism causes a point on the spectrometer entrance slit to be imaged into a line, elongating the

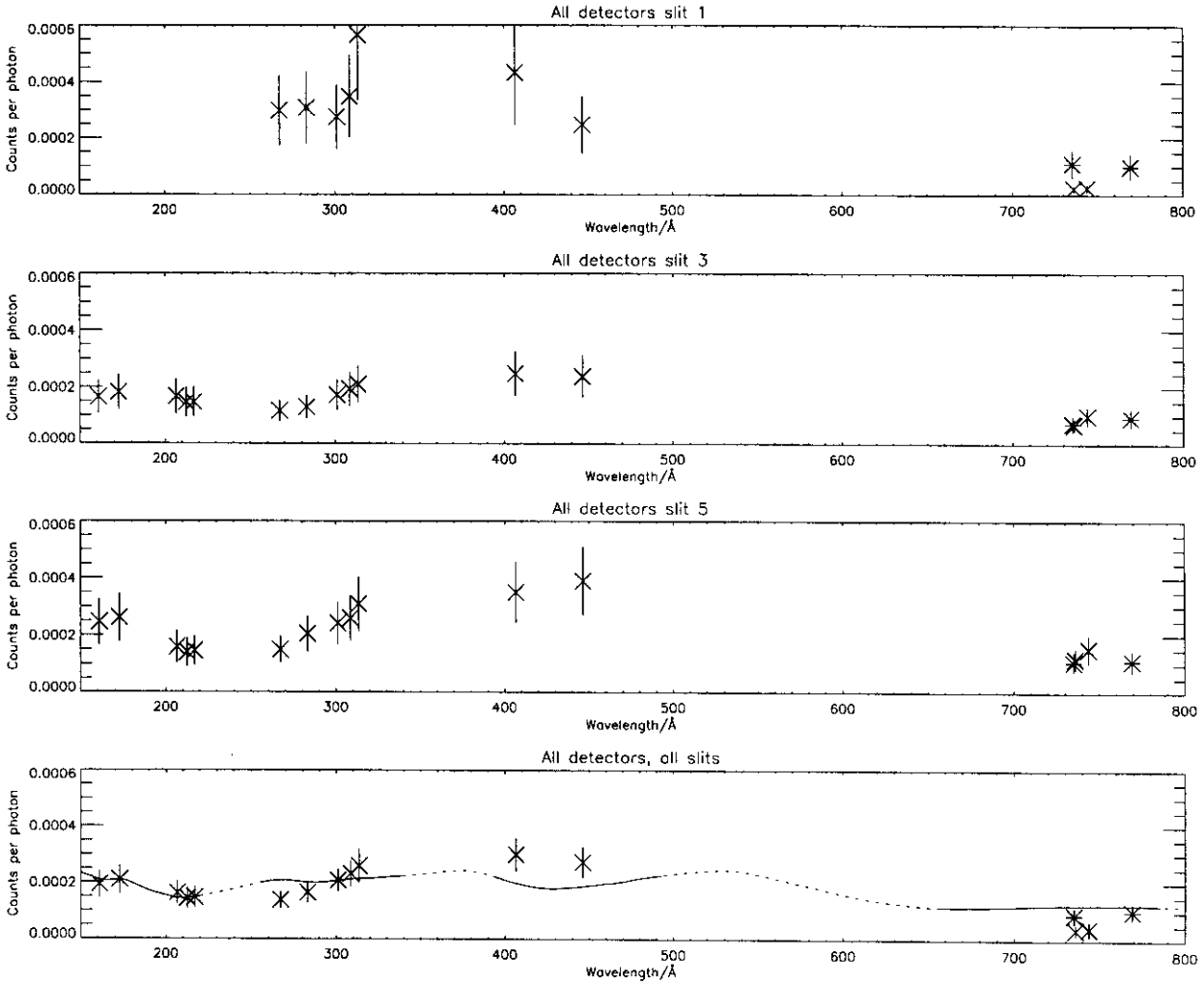

Figure 44: The measured sensitivity for slits 1, 3 and 5 and their weighted average as a function of wavelength. The Ar data for detector 4 are plotted with asterisks. The expected sensitivity divided by a factor of 20 is shown as the line, continuous over the wavelength ranges of the detectors and dotted otherwise.

Wavelength/Å	Counts/photon	Wavelength/Å	Counts/photon
Detector GI1		Detector GI2	
160.9	$(1.93\pm0.47)\times10^{-4}$	267.4	$(1.38\pm0.28)\times10^{-4}$
172.6	$(2.10\pm0.51)\times10^{-4}$	283.2	$(1.63\pm0.36)\times10^{-4}$
206.6	$(1.63\pm0.41)\times10^{-4}$	301.1	$(2.06\pm0.41)\times10^{-4}$
212.6	$(1.43\pm0.36)\times10^{-4}$	308.6	$(2.31\pm0.46)\times10^{-4}$
217.1	$(1.47\pm0.37)\times10^{-4}$	313.5	$(2.59\pm0.59)\times10^{-4}$
Detector GI3		Detector GI4	
406.5	$(2.99\pm0.60)\times10^{-4}$	731.7	$(8.92\pm1.84)\times10^{-5}$
446.4	$(2.73\pm0.54)\times10^{-4}$	769.2	$(1.02\pm0.21)\times10^{-4}$

Table 14: The measured grazing incidence sensitivities

image of the slit. Samson (1967) gives the length z of an astigmatic image as

$$z = l(\cos\beta/\cos\alpha) + L(\sin^2\beta + \sin\alpha\tan\alpha\cos\beta) = ll' + LL' \quad (11)$$

where α is the angle of incidence, β the angle of diffraction, L the length of the ruled lines illuminated and l the length of the entrance slit. The length of the grating illuminated is $2(R\cos\alpha\tan\theta/2)$ for a beam of angular divergence θ. For the illumination of the spectrometer by the laboratory source even with the longest slits the height of the astigmatic image is less than the active height of the detector (16.6 mm). For the case of illumination by the Sun, the height of the grating illuminated L is 2.26 mm. For the prime slits 1, 2 and 3 (25, 50 and 625 μ long respectively) the astigmatic image is, as in the laboratory case, shorter than the height of the detector. For slits 4, 5 or 6 which are 3 mm long (l = 3 mm) the quantities l' and L' and z (= ll' + LL) and the ratio of z divided by the height of the detector are given in table 15. For slits 4, 5 and 6 used with GI2, GI3 and GI4, this ratio when greater than 1 must be used as a correction factor for the loss of flux when applying the laboratory calibration to the solar case. A nominal ±10% uncertainty is taken for this correction.

Channel	Wavelength/Å	β	l'	L'	LL'+ll'	(LL'+ll')/16.6
GI1	151	78.7	2.141	3.058	13.40	0.81
	186	77.7	2.328	3.263	14.36	0.87
	221	76.8	2.496	3.423	15.22	0.92
GI2	256	76.0	2.644	3.563	15.99	0.96
	297	75.0	2.829	3.738	16.95	1.02
	338	74.2	2.976	3.877	17.69	1.07
GI3	393	73.0	3.195	4.083	18.81	1.13
	443	72.1	3.359	4.236	19.65	1.18
	493	71.2	3.522	4.389	20.48	1.23
GI4	656	68.5	4.005	4.838	22.95	1.38
	721	67.5	4.182	5.001	23.85	1.44
	785	66.5	4.358	5.162	24.74	1.49

Table 15: Evaluation of the length z of the astigmatic image for 3 mm high slit and solar illumination of the grazing incidence spectrometer.

For the laboratory calibration the voltage on the NIS VDS detector was at its maximum to allow the weakest lines from the hollow cathode source to be detected, while for solar observations it is lower. Changing the operating voltage changes the amplification of the detector and thus its throughput which is defined as the number of analogue-to-digital conversions for each photon interacting with MCP. The voltage applied in the laboratory was 990 V with measured throughput of 35.0±3.8 while in flight the voltage applied is 756 V with measured throughput of 2.43 ± 0.27. The throughput ratio and its ±16% uncertainty must be considered when applying the NIS laboratory sensitivity to solar observations.

The application of the results of the laboratory calibration to solar observations divides into two cases, depending on whether an absolute or a relative calibration is required.

For an absolute calibration for the intensity of a line, all the various factors with their uncertainties must be included. The first factor is the effective aperture at the particular scan mirror position used, interpolated from the data of table 5 for the relevant spectrometer. The second factor is the conversion of counts to photons. The uncertainty for this conversion must have added to it the uncertainty associated with the calibration of the source ($\pm 7\%$). The third factor, for the GIS is the astigmatism factor if required and for the NIS is the VDS throughput change factor. These factors must be applied to the counts in the observed line with associated uncertainty (having taken into account the subtraction of any background). The absolute calibration is applied using the CDS analysis software. In addition the history of the change in the performance of the relevant detector since solar observations started must and can be allowed for using the same software.

A relative calibration is required when, say, taking the ratio of two line intensities. There are several cases to consider. If the lines are one in a GIS waveband and the other in a NIS waveband then each line has the calibration and uncertainty as for the absolute intensity case. This is because the GIS and NIS are essentially independent spectrometers. Indeed, they are never used simultaneously. For the case of ratios of lines between wavebands of the GIS, the aperture factor cancels while the counts to photon conversion including the source uncertainty for each waveband must be included as each waveband was calibrated independently. The astigmatism factor will be needed as appropriate. For a ratio between lines in the NI1 and NI2 wavebands the aperture factors and their uncertainties will be needed as well as the counts to photon conversion with their uncertainties. As different parts of the same detector are used, the throughput factor cancels and need not be considered. Lastly, if the lines are in the same waveband i.e. wholly within one of GI1, GI2, GI3, GI4, NI1 or NI2, the aperture factor cancels. Similarly the lamp calibration uncertainty need not be added. The astigmatism factor will be needed for use of slit 4, 5 or 6 with GI2, GI3 or GI4. For the NIS the throughput change factor does not apply.

10 Conclusions

Following a brief overview of CDS and the calibration source, the laboratory calibration of CDS has been presented. The measurements of the aperture size, the line widths, the wavelength calibration and the all important sensitivity have been described. Uncertainties have been estimated and the application of the calibration described. The overall uncertainty in the absolute responsivity calibration for the GIS is around $\pm 25\%$ and for the NIS is around $\pm 30\%$. This compares very favourably with the previously flown solar EUV satellite instrumentation.

11 Acknowledgements

The help of many colleagues at the institutes belonging to the CDS consortium is acknowledged. Without their skills and enthusiasm, this work could not have been accomplished.

12 References

Breeveld A.A., Edgar M.L., Smith A., Lapington J.S. and Thomas P.D., Rev. Sci. Instr. **63**, 1 (1992).

Breeveld A.A., *Ultraviolet Detectors for Solar Observations on the SOHO Spacecraft*, University of London Ph.D. Thesis (1995).

Browning R., Kent B.J. and Richards A.G., private communication (1997).

Danzmann K., Günther M., Fischer J., Kock M. and Kühne M, Appl. Opt. **27**, 4947 (1988).

Geesmann H., Hanne G.F., Stauffer A.D. and Stauffer J.A., Nucl. Inst. and Meth. **A307**, 413 (1991).

Harrison R.A., et al., Solar Physics **162**, 233-290 (1995).

Hollandt J., *Strahlungsnormale für die solare Spektroradiometrie im Vakuum-UV*, Technischen Universität Berlin (1994).

Hollandt J., Kühne M., Huber M.C.E. and Wende B., Astron. and Astrophys. Suppl. Ser. **115**, 561 (1996a).

Hollandt J., Kühne M. and Wende B., Appl. Opt. **33**, 68 (1994).

Hollandt J., Schühle U., Paustian W., Curdt W., Kühne M., Wende B and Wilhelm K., Appl. Opt. **35**, 5125 (1996b).

Kent B.J., Carter M.C. and Read P.D. , in preparation (1999).

Lidiard K.A., private communication (1995).

Lidiard K.A and Gray P.F., Opt. Eng. **36**, 2311 (1997).

Lynch D.W. and Hunter W.R., in *Handbook of Optical Constants of Solids*, edited by Palik E.D. (Academic Press, Florida 1985), p275.

McConkey J.W., Crouch T. and Tomc J., Appl. Opt. **21**, 1643 (1982).

Samson J.A.R., *Techniques of Vacuum Ultraviolet Spectroscopy*, J. Wiley and Sons, Inc., New York (1967).

Thomas R.J., private communication (1994).

Thompson W.T., Poland A.I., Sigmund O.W., Swartz M., Leviton D.B. and Payne L.J., SPIE Proc. **1743**, 464 (1992).

Tomc J., Zetner P., Westerveld B. and McConkey J.W., Appl. Opt. **23**, 656 (1984)